



Remote Sensing of Atmospheric and Ionospheric Signals Prior to the Mw 8.3 Illapel Earthquake, Chile 2015

MOHAMMAD REZA MANSOURI DANESHVAR¹  and FRIEDEMANN T. FREUND^{2,3,4}

Abstract—In the present study, a number of atmospheric and some ionospheric anomalies are analyzed, which were recorded prior to the Mw 8.3 Illapel earthquake of September 16, 2015. This very large earthquake occurred in Central Chile, close to the coast, as the result of thrust faulting on the interface between the Nazca Plate and South American continent. Using remotely sensed data extracted from NASA/Giovanni, NOAA/NCEP, and NOAA/NGDC, atmospheric and ionospheric anomalies were observed that co-registered 35–40 and 25–30 days prior to the main shock, respectively. With reference to long-term time series over the epicentral area, significant atmospheric anomalies were recorded for cloud cover, geopotential height, precipitation rates, surface air pressure, omega, stream function, and wind vectors—all in the time window of August 5–10, 2015, 35–40 days prior to the main shock. Anomalous TEC maps were recorded for the same time period. Satellite images indicate the formation of an unusual cyclone, presumably triggered by air turbulences and abnormal atmospheric conditions over the epicentral area, including strong vertical winds. Data from the Jicamarca radio observatory in Peru, more than 2000 km to the North, reveal anomalous ionospheric variations on August 15–20, 2015 with respect to international reference ionosphere thickness parameters and the altitude of the F layer. The observed anomalies are consistent with processes that occur at the ground-to-air interface due to the stress activation of peroxy defects in the hypocentral volume. The flow of positive hole charge carriers to the Earth surface expected to have led to massive air ionization, generating at first primarily positive airborne ions, then negative air ions plus ozone. Understanding the sequence of processes inside the Earth's crust and at the ground-to-air interface provides information not previously available about the causal and temporal linkages between the various pre-earthquake phenomena and the future seismic event.

Key words: Illapel earthquake, Chile, Atmospheric anomalies, Ionospheric anomalies, Satellite observations, Remote sensing, Earthquake precursors, Peroxy defects, Positive hole charge carriers.

1. Introduction

Multisource remote-sensing techniques provide the opportunity to recognize correlations between seismic activity and non-seismic phenomena (Alvan et al. 2014). Phenomena that precede major earthquakes have been reported from essentially all seismically active regions of the world (Mansouri Daneshvar et al. 2014). A large effort has been ongoing for many years to identify possible short-term precursors, including a range of atmospheric and ionospheric anomalies (Pířa et al. 2011). In fact, perturbations in the atmosphere and ionosphere have been widely reported in recent years as bona fide pre-earthquake (pre-EQ) signals. Synchronized and co-located pre-EQ anomalies have been registered in different geo-climatic regions using different remote-sensing techniques (Pulinets et al. 2009).

The goal of the present paper is twofold: (1) explore the anomalous atmospheric and ionospheric phenomena observed prior to the very large Chilean, subduction zone related, Mw 8.3 Illapel earthquake of 2015 and (2) examine the process or processes inside the rock column that drive these atmospheric and ionospheric anomalies.

Earthquakes are—in essence—mechanical events. Prior to any earthquake, tectonic forces deep in the Earth subject rocks to increasing levels of stress and cause them to eventually undergo catastrophic rupture. If pre-rupture processes are accompanied by

This paper is part of the article collection on “Illapel, Chile, Earthquake on September 16th, 2015”.

¹ Department of Geography and Natural Hazards, Research Institute of Shakhes Pajouh, Isfahan, Iran. E-mail: mrm_daneshvar2012@yahoo.com; m.r.m.daneshvar@bpbshakhespajouh.ac.ir

² NASA Ames Research Center, Code SCR, Moffett Field, Mountain View, CA 94035-1000, USA. E-mail: friedemann.t.freund@nasa.gov

³ Carl Sagan Center, SETI Institute, Mountain View, CA 94043, USA.

⁴ Department of Physics, San Jose State University, San Jose, CA 95192-0106, USA.

atmospheric and ionospheric manifestations, it stands to reason that the mechanical action inside the rock column causes some non-mechanical reactions which manifest themselves at the Earth surface and above, leading to the atmospheric and ionospheric anomalies. From a physics perspective the only non-mechanical reactions that can be expected to reach this far and to cause secondary processes in the atmosphere and ionosphere are electrical in nature.

2. Materials and Methods

2.1. Study Area

The September 16, 2015 Mw 8.3 Illapel earthquake resulted from thrust faulting along the boundary between the oceanic Nazca plate and the South American continent. It occurred in central Chile (31.57S, 71.67W), 48 km west of Illapel at a depth approximately 24 km (United States Geological Survey 2015). In recent years, extensive seismic precursory activity had been recognized along this boundary by Píša et al. (2011), Zhang et al. (2011), Galvan et al. (2011), Ho et al. (2013b), Pulnits and Davidenko (2014), Alvan et al. (2014), Yagi et al. (2014) and Gusman et al. (2015). The Nazca plate is moving towards the east–northeast at a velocity of 74 mm/year with respect to the South American continent. The subduction begins at the Peru–Chile Trench, 85 km to the west of the Mw 8.3 Illapel epicenter. According to the United States Geological Survey (USGS) archive (<http://www.earthquake.usgs.gov/earthquakes/search>), an earthquake preparation zone¹ marked by about 565 earthquakes ($M > 3$) during August and September 2015 preceded the Illapel earthquake extending over a wide area, 20–40S, 60–80W (Fig. 1).

¹ The Earthquake Preparation Zone was defined by Dobrovolsky et al. (1979) from empirical observations as a circle around the epicenter of an earthquake assuming that stresses would be able to couple this far within the crust. With the radius of this circle being given as $r = 10^{0.43M}$ km, where M is the magnitude. For the Illapel Mw 8.3 event the Earthquake Preparation Zone radius would have reached as far as ~ 3700 km.

2.2. Data Preparation

To detect temporal and spatial atmospheric and ionospheric variations over the earthquake preparation zone of the Illapel event, remote-sensing data were compiled from several websites. To recognize temporal anomalies, daily time series was constructed from two data sources on the web to access, visualize, and analyze the atmospheric data as below. Several variables were extracted from GIOVANNI² via <http://www.giovanni.sci.gsfc.nasa.gov/giovanni>, including the geopotential height,³ the precipitation rate, cloud cover, and tropospheric ozone column thickness. GIOVANNI ver. 4 is an online data source developed and maintained at NASA GES DISC.⁴ Other variables, including mean daily u-wind⁵ and v-wind⁶ speed, surface pressure, omega,⁷ and stream function, were extracted from the APDRC LAS⁸ data set via <http://apdrc.soest.hawaii.edu/las/getUI.do>. LAS ver. 7 is a highly configurable web server designed by the NOAA PMEL⁹ site to provide flexible access to geo-referenced scientific data.

To identify any significant anomalous trends, all daily time series data were analyzed for a period of 6 years (2010–2015). The intervals were shifted between August and September 2015. Data anomalies were detected using $\mu \pm 2\sigma$ (mean \pm double standard deviation) based on the long-term reference level (1981–2010). Anomalies were defined as the deviation of the mean value from a reference field in a time period (Ouzounov et al. 2007).

To investigate the spatial variability, daily mean composites data were compiled via <http://www.esrl.noaa.gov/psd/data/composites/day>. Daily composites

² Geospatial Interactive Online Visualization and Analysis Infrastructure.

³ In atmospheric sciences the term of geopotential height is defined as the actual height of a pressure surface above mean sea-level. Geopotential heights are lower in cold air masses and higher in warm air masses (<http://www2010.atmos.uiuc.edu>).

⁴ National Aeronautics and Space Administration, Goddard Earth Sciences Data and Information Services Center.

⁵ Zonal vector of wind refers to the east–west direction.

⁶ Meridional vector of wind refers to the north–south direction.

⁷ Air vertical motion.

⁸ Asia Pacific Data Research Center Live Access Server.

⁹ National Oceanic and Atmospheric Administration, Pacific Marine Environmental Laboratory.

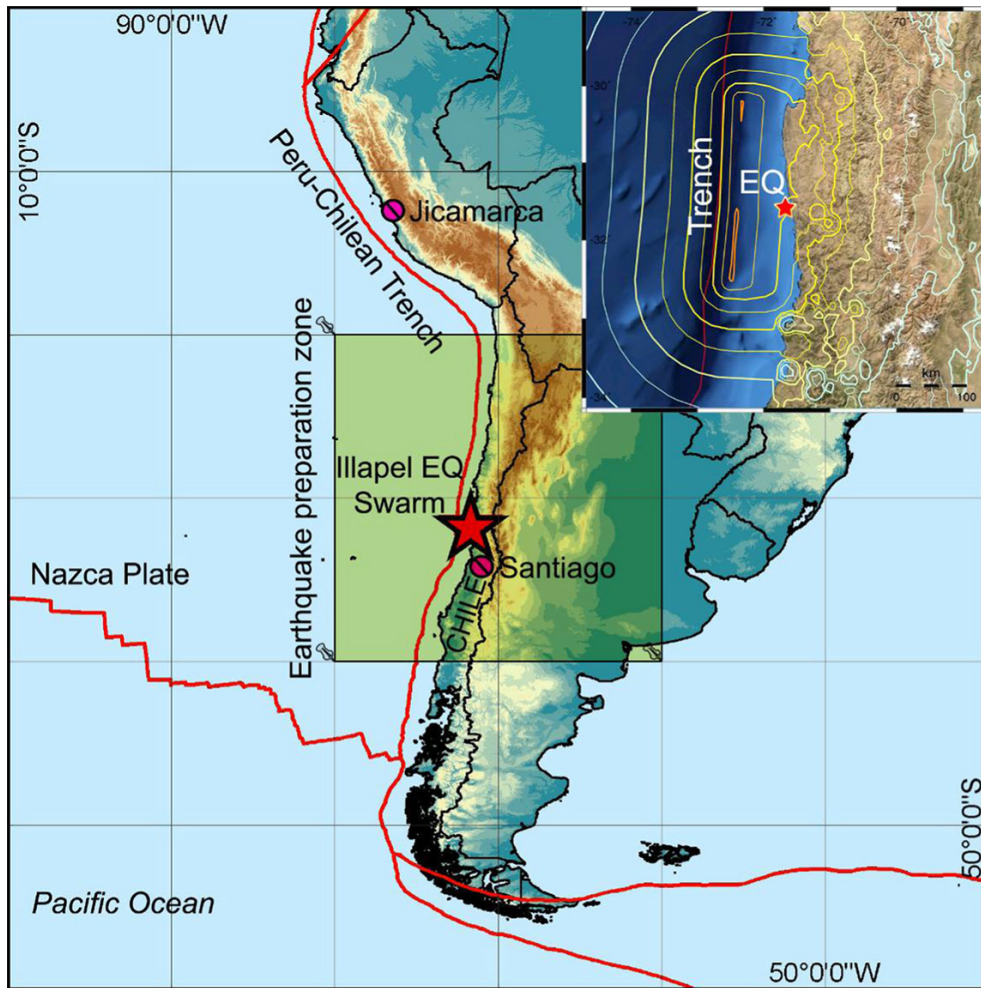


Figure 1

General study area: epicenter of Illapel earthquake swarm on September 16, 2015, earthquake preparation zone and adjacent ionospheric monitoring stations of Jicamarca radio observatory station in Peru and IGS stations of Santiago and Iquique in Chile

of the means and the anomalies of the atmospheric variables were derived from the NOAA, NCEP¹⁰ reanalysis, and other datasets. To study cloud patterns and cloud coverage, GOES TIR¹¹ data were used with GOES TIR high-resolution radiometer imagery data from 3 h averages in the thermal infrared band (10.2–11.2 μm) of the GOES East 075.0W Quicklook Archive via <http://www.sat.dundee.ac.uk/geobrowse/geobrowse.php>. Anomalous ionosphere perturbations

were derived from SPIDR¹² via <http://spidr.ngdc.noaa.gov/spidr> for the Jicamarca radio observatory in Peru (11.95S, 76.87 W). SPIDR ver. 5 is an online data system developed and maintained by NOAA and NGDC.¹³

Furthermore, IGS¹⁴ products were considered via <http://igs.org/network> to access GPS¹⁵ observations by the ionosphere-monitoring station in Santiago

¹⁰ National Oceanic and Atmospheric Administration, National Centers for Environmental Prediction.

¹¹ Geostationary Operational Environmental Satellite Thermal Infrared.

¹² Space Physics Interactive Data Resource.

¹³ National Oceanic and Atmospheric Administration, National Geophysical Data Center.

¹⁴ International GNSS Service.

¹⁵ Global Positioning System.

(33.15S, 70.66W) in Chile. The IGS global system of satellite tracking stations, data centers, and analysis centers puts high-quality GPS data and data products online in near-real time to meet the objectives of a wide range of scientific and engineering applications and studies.

Daily TEC¹⁶ time series was explored using the final product of GIMs¹⁷ data over the Santiago region by the IGS ionosphere-working group via <http://igsiono.uwm.edu.pl>. Reference TEC values were provided by IONEX¹⁸ that supports the exchange of TEC maps in geographic grids (Schaer et al. 1998). The GIMs were constructed from a $5^\circ \times 2.5^\circ$ (longitude, latitude) grid with a time resolution of 2 h. The GIMs were generated on a daily basis using data from about 150 GPS sites. TEC maps were retrieved from the IGS-associated analysis centers CODE,¹⁹ ESOC,²⁰ JPL,²¹ and UPC.²² Daily TEC data were obtained using DRAWING-TEC²³ data provided by the NICT²⁴ world data center via <http://seg-web.nict.go.jp/GPS/DRAWING-TEC>. For the temporal study of geomagnetic storms, the Kp indices were extracted from NOAA SWPC²⁵ via http://www.ngdc.noaa.gov/stp/GEOMAG/kp_ap.html. The Kp index, a global indicator of geomagnetic storms (Mukhtarov et al. 2013), can range from 0 to 9, where 0 means that very little geomagnetic activity and 9 means extreme geomagnetic storming. To process the data, SPSS and ArcGIS tools were used.

¹⁶ Total Electron Content.

¹⁷ Global Ionosphere Maps.

¹⁸ IONosphere map EXchange.

¹⁹ Center for Orbit Determination in Europe, University of Berne, Switzerland.

²⁰ European Space Operations Center of ESA, Darmstadt, Germany.

²¹ Jet Propulsion Laboratory, Pasadena, California, USA.

²² Technical University of Catalonia, Barcelona, Spain.

²³ Dense Regional And Worldwide International GNSS-TEC observation.

²⁴ National Institute of Information and Communications Technology, Japan.

²⁵ Space Weather Prediction Center.

3. Results and Discussion

3.1. Anomalous Atmospheric and Ionospheric Phenomena

In a paper on the detection of the short-term atmospheric precursors prior to the April 16, 2003 M 7.8 Saravan earthquake in Iran, Mansouri Daneshvar et al. (2014) noted that, in the chain of air turbulences, abnormal thunderstorm and atmospheric anomalies prior to the main shock, gas exhalation from the ground and anomalous cloud coverage may be common precursors. Thus, to investigate the temporal time series of atmospheric anomalies, the first task is to focus on the cloudiness and trace gas release using available parameters.

According to the time series of the cloud cover and of the ozone total column thickness, both showed deviations on August 5–10, 2015 (Figs. 2, 3). To demonstrate that these anomalies were real and significant, the deviations were examined over much longer time series intervals. Based on daily time series data for 6 years (2010–2015), the deviations on August 5–10 were real and significant, reinforcing the finding that both indicators suddenly and jointly increased 35–40 days before the Illapel earthquake of September 16, 2015. Specifically, while the cloud coverage increased to near to 70 % over the time period of August 5–10, the tropospheric ozone increased to nearly 350 DU (Dobson Units). Simultaneously, a significant increase by nearly 2.5 DU is seen in the sulfur dioxide time series (Fig. 4), indicating that cloud coverage, ozone, and sulfur dioxide show closely the same behavior 35–40 days before the main shock. By contrast, the carbon monoxide total column values do not exhibit abnormal deviations in the same time period before the Illapel earthquake (Fig. 5). The observed variation of CO during the months of September to November can be attributed to the usual semi-annual cycle.

There are reports on elevated ozone concentrations remotely detected before strong earthquakes in Central Asia (Tyrtysnikov 1996) and in the Nepal region (Ganguly 2016). To account for the ozone formation and the concomitant perturbations in the atmosphere and ionosphere, an emanation of trace gases has been proposed, in particular of radon,

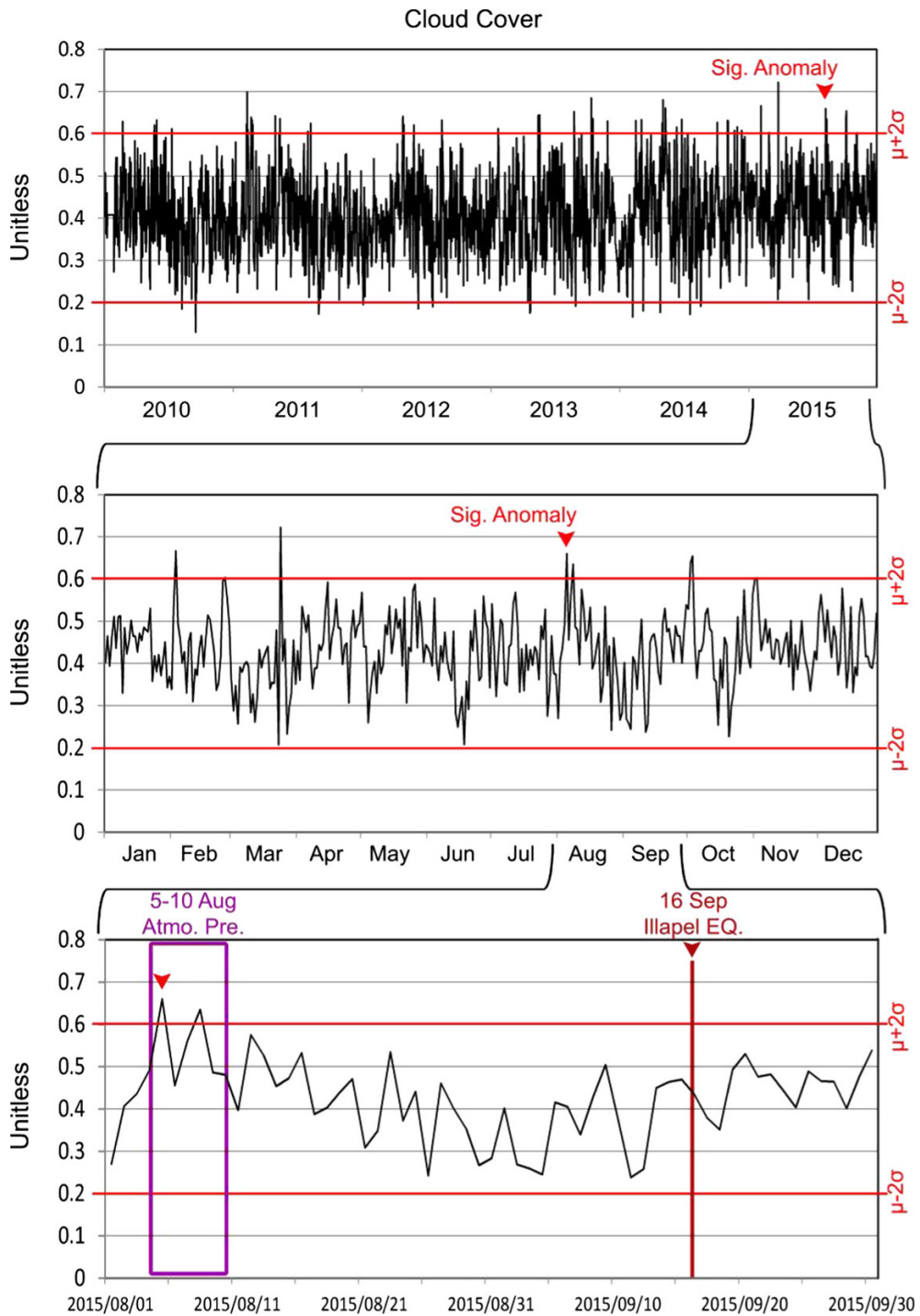


Figure 2
Long-term time series of daily cloud coverage over the epicentral area and the signals of significant anomalies, extracted from NASA/ Giovanni

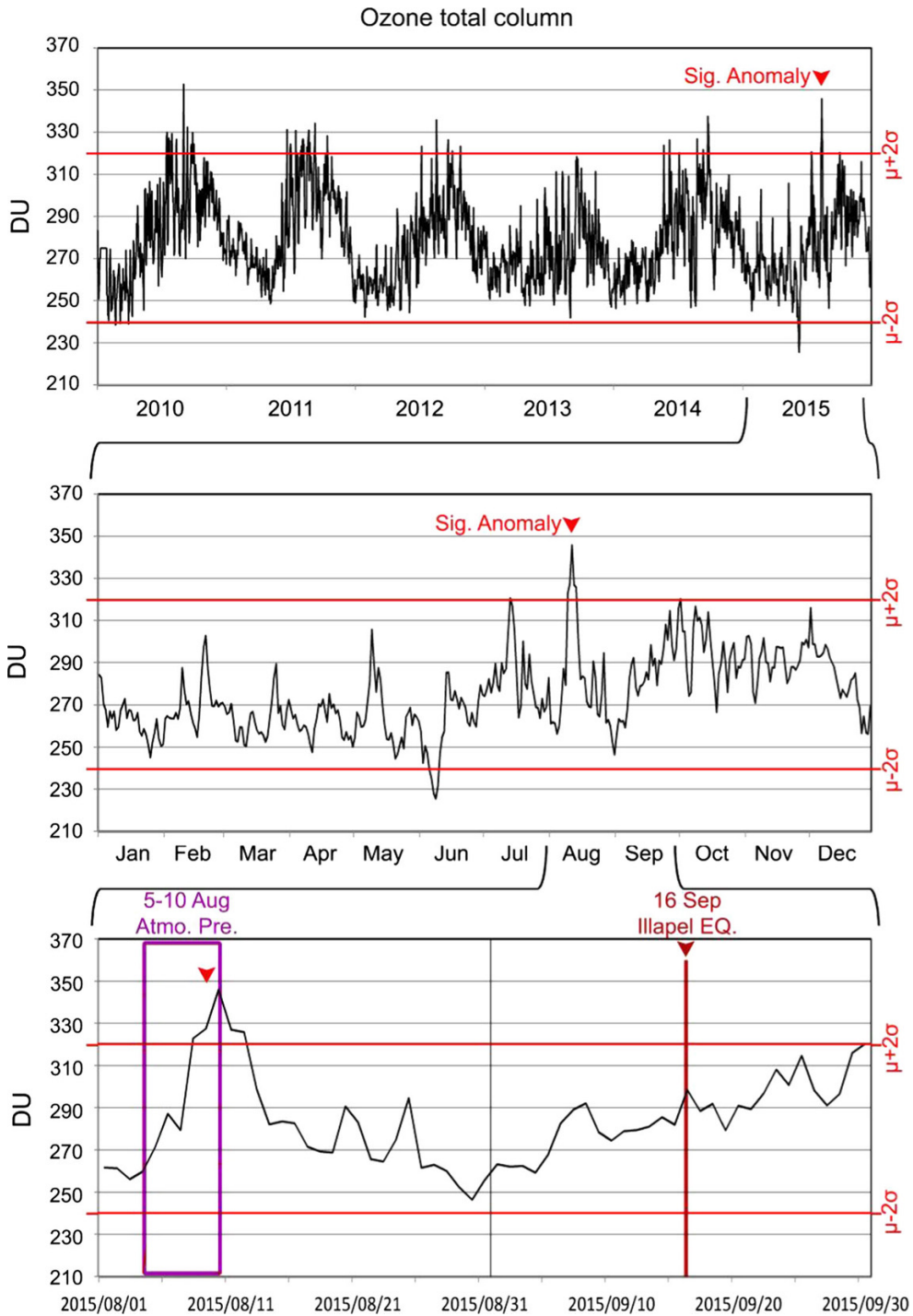


Figure 3
Long-term time series of daily ozone total column over the epicentral area and the signals of significant anomalies, extracted from NASA/
Giovanni

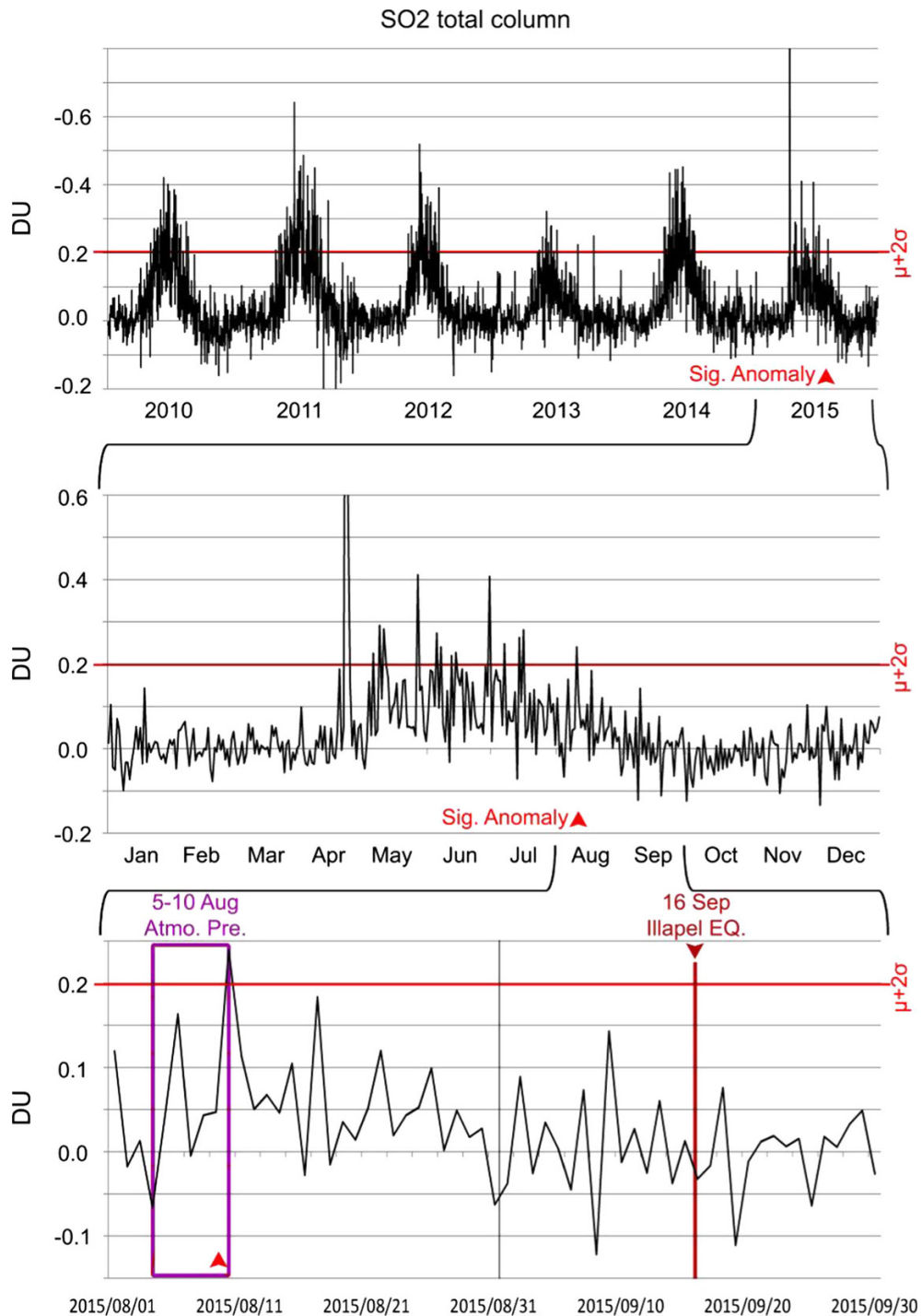


Figure 4

Long-term time series of daily sulfur dioxide total column over the epicentral area and the signals of significant anomalies, extracted from NASA/Giovanni

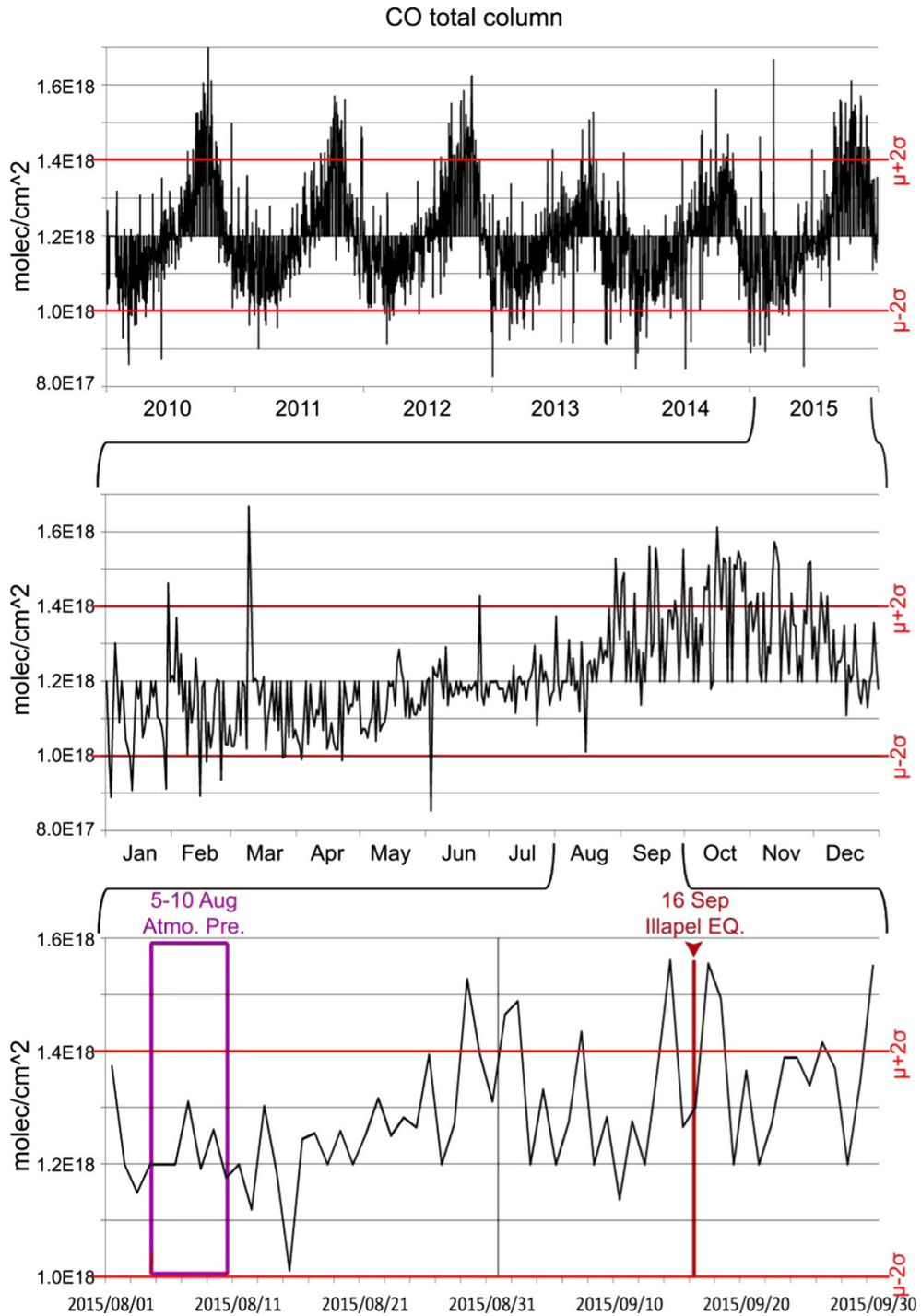


Figure 5

Long-term time series of daily carbon monoxide total column over the epicentral area and the signals of significant anomalies, extracted from NASA/Giovanni

released from the ground due to the build-up of stress. Radon would ionize the air, causing ozone to form and moisture to condense on the airborne ions, leading to a thermal updraft due to the attendant release of latent heat (Klimenko et al. 2011; Pulinets et al. 2014; Qin et al. 2012; Walia et al. 2006).

Based on laboratory experiments that demonstrated massive air ionization at the rock-to-air interface when rock samples are stressed at one end, Freund et al. (2009) proposed a fundamentally different process to generate positive and negative airborne ions at the Earth ground-to-air interface prior to major seismic activity.

This process starts with the stress activation of peroxy defects in the rocks in and around the hypocenter deep below, called the “source volume”. Peroxy defects exist in igneous minerals in crystalline basement rocks (Freund and Freund 2015b). Their activation leads to the generation of highly mobile electronic charge carriers, called “positive holes”, which have the remarkable ability to flow out of the source volume, spreading into and through less stressed and unstressed rocks, traveling fast and far, meters in laboratory experiments and kilometers to tens of kilometers in the field (Freund 2011, 2013; Scoville et al. 2015). When positive hole charge carriers arrive at the Earth surface, they set up microscopic but steep electric (E) fields (King and Freund 1984). When the E fields reach values in the range of 10^6 V m^{-1} , they begin field-ionizing air molecules, in particular O_2 , which has the lowest ionization potential of the common atmospheric gases, 12.07 eV. This leads to the formation of airborne O_2^+ ions.

Upon further influx of positive holes to the surface, the E fields reach values sufficient to accelerate adventitious free electrons, always available in the air due to cosmic rays, radon, and natural radioactivity from the ground, to energies high enough to impact-ionize neutral gas molecules. This process then triggers corona discharges, which produce free electrons that attach themselves to neutral gas molecules leading to a massive production of airborne negative air ions. In addition, corona discharges are highly efficient to produce ozone, O_3 .

Freund (2013) further suggested that, when positive airborne ions, such as O_2^+ , are generated at

ground level, they will rise upward not only because of incipient moisture condensation and its release of latent heat, causing a thermal updraft, but also because of a different process that had not yet been widely considered: due to the polarity of the Global Electric Field positive airborne ions should rise upward towards the ionosphere.

Conventionally, the polarity of the Global Electric Field is assumed to be given by the surface of the Earth being negative and the lower edge of the ionosphere being positive (Takagi and Kanada 1972; Sapkota and Varshneya 1990; Rycroft et al. 2008; Singh et al. 2011). The rationale behind this polarity is that, as lightnings strike the Earth’s surface, they would deposit negative charge into the ground negatively and that positive air ions drifting upward above large thundercloud systems would cause the lower edge of the ionosphere to become positively charged (Aleksandrov et al. 2001; Blakeslee et al. 1989; Rycroft and Harrison 2012; Thomas et al. 2009). By contrast, the recognition that the Earth surface appears to be always positive due to the presence of peroxy defects in crustal rocks (Freund and Freund 2015b) and to the activation of positive hole charge carriers by tectonic stresses (Freund et al. 2009; Freund 2011, 2013) calls into question this polarity of the Global Electric Field.

If the Earth surface is positive and the lower edge of the ionosphere negative, the estimated 250,000–500,000 V potential difference to the Earth’s surface will provide for an effective transport mechanism for positive airborne ions, drifting upward in the vertical E field. This process links positive air ionization at ground level to the perturbations noted in the electron concentration in the ionospheric plasma widely known as TEC (Total Electron Content) anomalies (Sapkota and Varshneya 1990; Liu et al. 2004; Ho et al. 2013a). Conditions created by the suspected massive air ionization are expected to affect the entire epicentral area, which exhibits atmospheric thermal anomalies, vertical winds, aerosol concentration, and other meteorological phenomena (Freund 2003).

To detect the main meteorological signals, geopotential heights data were considered first. Plotting this variable for the area around the Illapel September 16, 2015 earthquake reveals a geopotential height

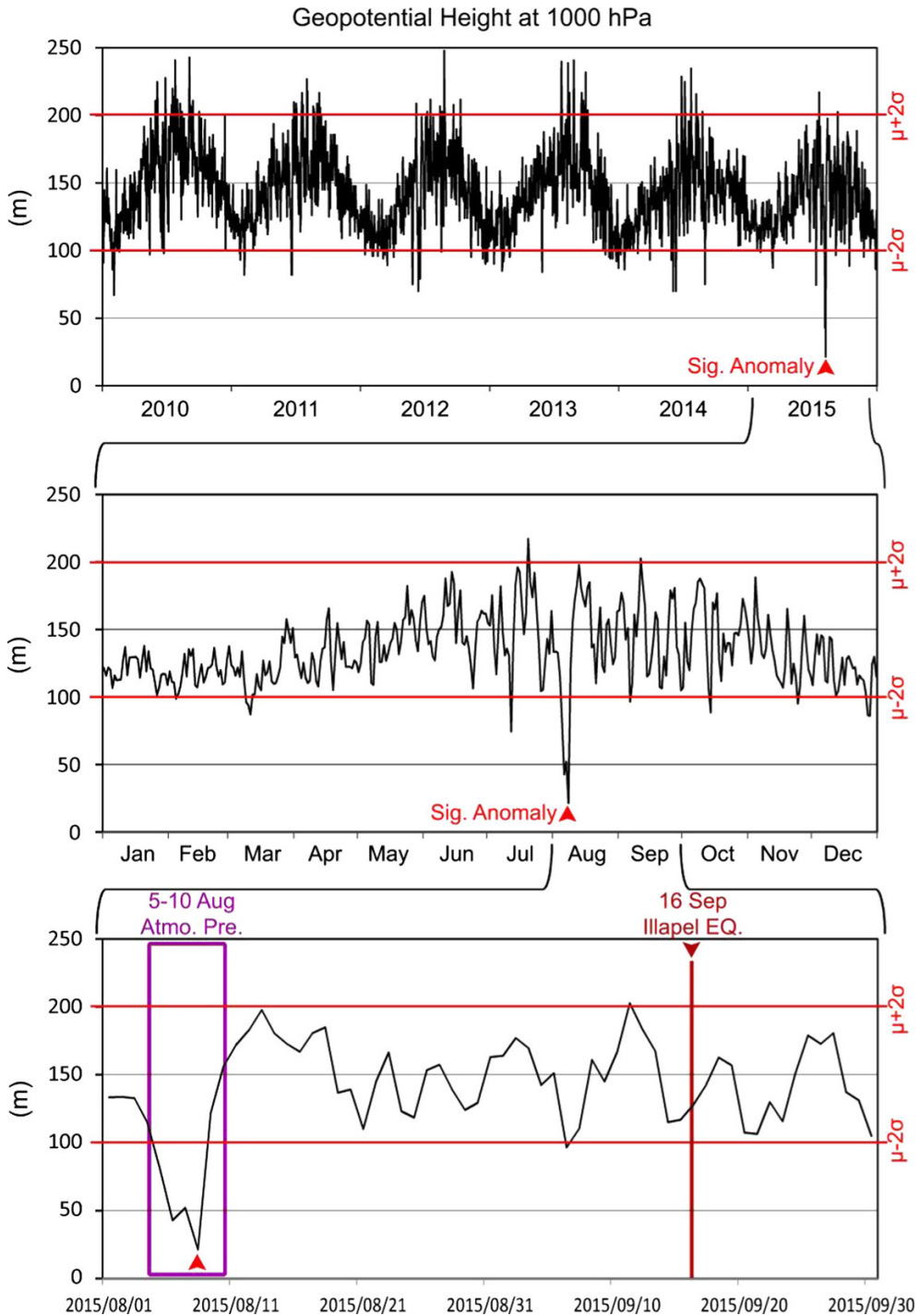


Figure 6

Long-term time series of daily geopotential height at 1000 hPa over the epicentral area and the signals of significant anomalies, extracted from NASA/Giovanni

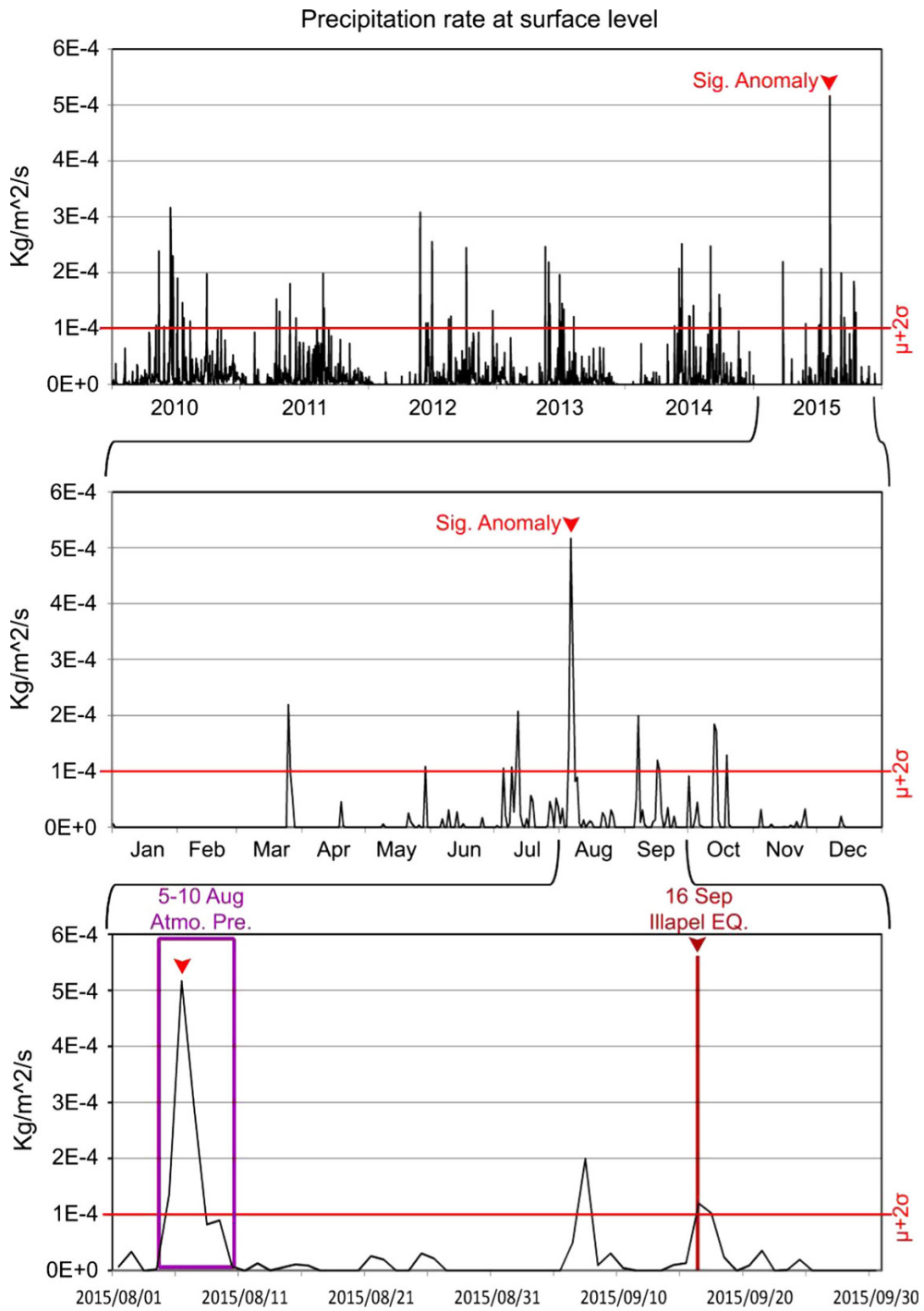
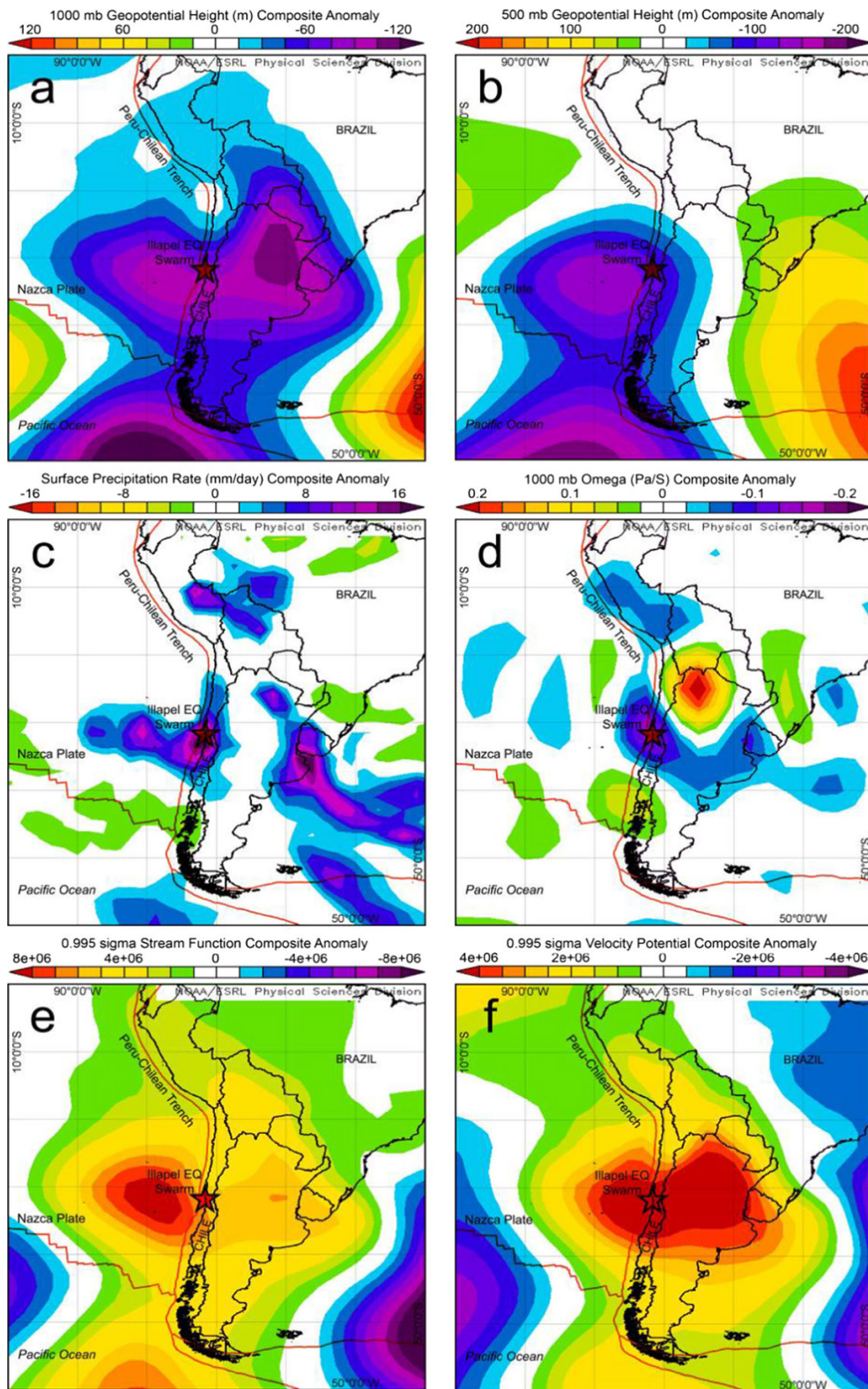


Figure 7

Long-term time series of daily precipitation rate at surface level over the epicentral area and the signals of significant anomalies, extracted from NASA/Giovanni



◀Figure 8

Long-term composite anomaly of atmospheric variations at surface level on August 5–10, 2015 including **a** geopotential height at 1000 hPa, **b** geopotential height at 500 hPa, **c** precipitation rate, **d** omega, **e** stream function, and **f** velocity potential extracted from NOAA/NCEP

anomaly (~ 30 m) on August 5–10 coincident with the aforementioned trace gas anomalies (Fig. 6). Figure 7 shows an anomalous 5 mm/day increase in the precipitation rate at the same time. In addition, an abnormal cyclone is seen over the epicentral area on August 5–10 coupled to increased humidity and precipitation.

To validate the cyclogenesis, the anomalies of the 1000 and 500 geopotential height isobars, precipitation rate, omega (vertical motion of air), surface stream function, and velocity potentials are surveyed in Fig. 8. Omega refers to air vertical motion that is made up of two terms: an element due to the rate of change of the vorticity advection with height and an element due to horizontal thermal advection. A negative value defines air upward motion (ascent), and a positive value defines air downward motion (subsidence). In addition to a distinct positive anomaly of precipitation rate, Fig. 8 reveals the lowest negative value indicating a powerful air upward motion of the air over the epicentral area. Hence, the stream function and velocity potential as the flow characteristics represent an increasing anomaly.

These simultaneous variations reveal the abnormal synoptic scale thunderstorm activities and air turbulences on August 5–10, over the epicentral area of the Mw 8.3 Illapel earthquake. In particular, the geopotential height maps show the cyclone with abnormal central heights of -100 to -150 m. At the same time, anomalous maxima of the precipitation rate and of omega is observed over the wider earthquake preparation zone (Fig. 8). Based on the time series, these dynamic anomalies are associated at a 0.995 sigma level with surface pressure and omega anomalies (Figs. 9, 10). In addition, the stream function and velocity potential anomalies indicate abnormal dynamics in the atmosphere over the study area (Fig. 11). Specifically, the earthquake preparation zone was marked by abruptly decreasing air pressure creating vertical winds, or created by vertical winds, about 35–40 days prior to the Mw 8.3

Illapel earthquake. To identify horizontal flow of air masses, the variations of the u-wind and the v-wind vectors were investigated at surface level (Figs. 12, 13).

U-wind as zonal vector of wind refers to the east–west direction, while v-wind as meridional vector of wind refers to the north–south direction. This analysis reveals that the u-wind increased suddenly, while the v-wind decreased. The zonal vector increased abruptly by as much as 8 m/s. The wind direction had an anomalous component from the west to east, perpendicular to the Peru–Chilean trench direction.

Earlier reports (Pulinets and Ouzounov 2011) did indicate that heat flux differences tended to develop between active faults and areas far from the faults, leading to air movements and air turbulences over the epicentral areas of large earthquakes. Increases of wind speeds prior to major earthquakes has been reported by Hsu et al. (2010) and Mansouri Daneshvar et al. (2014). However, in the present study, additional evidence is presented for these atmospheric anomalies and air turbulences, including cloud coverage and air circulation using the GOES thermal infrared data within August 5–10, 2015 (Figs. 14, 15). These figures represents two selected image windows for each day. The satellite data show a sudden, almost catastrophic formation of a cyclone over the western part of the Mw 8.3 epicentral region (~ 32 S, ~ 80 W). This cyclone appeared on August 7–8, 2015 and was stationary over the Nazca plate boundary during the next few days. The associated air turbulences and circulation pattern are consistent with the aforementioned atmospheric variables.

Finally, ionospheric perturbations are included in this analysis, because ionospheric anomalies are often mentioned in the literature on earthquake precursors. Prior to major earthquakes, the ionosphere reportedly often displays remarkable perturbations (Pulinets and Boyarchuk 2004). In the case of Mw 8.3 Illapel event, to differentiate local ionosphere perturbations from geomagnetic storm disturbances, the ionospheric indices were obtained from the nearest radio observatory Jicamarca (Fig. 16) over 2000 km to the north of the Illapel epicenter. Relevant parameters were

²⁶ International Reference Ionosphere.

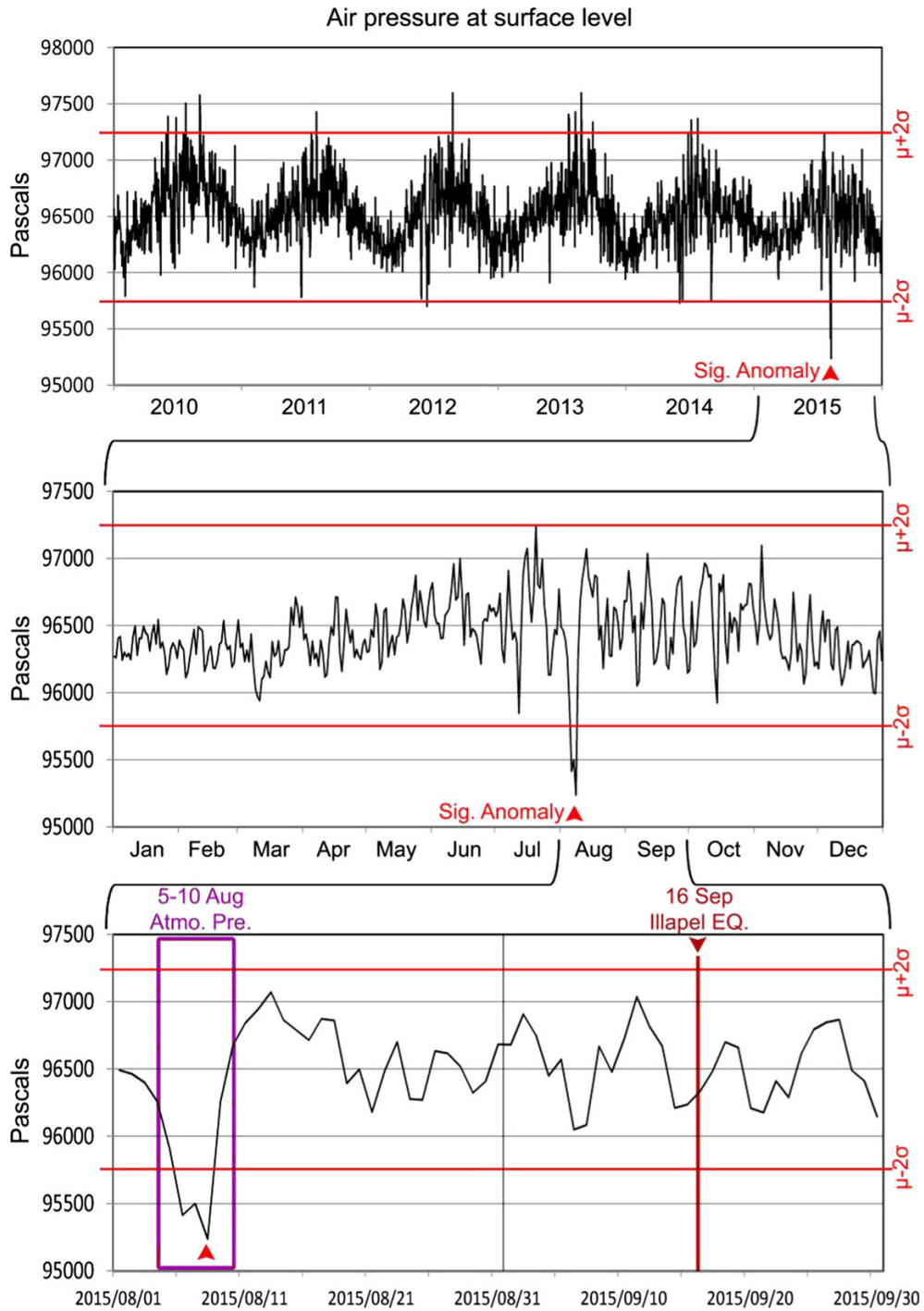


Figure 9

Long-term time series of daily air pressure at surface level over the epicentral area and the signals of significant anomalies, extracted from NOAA/PMEL

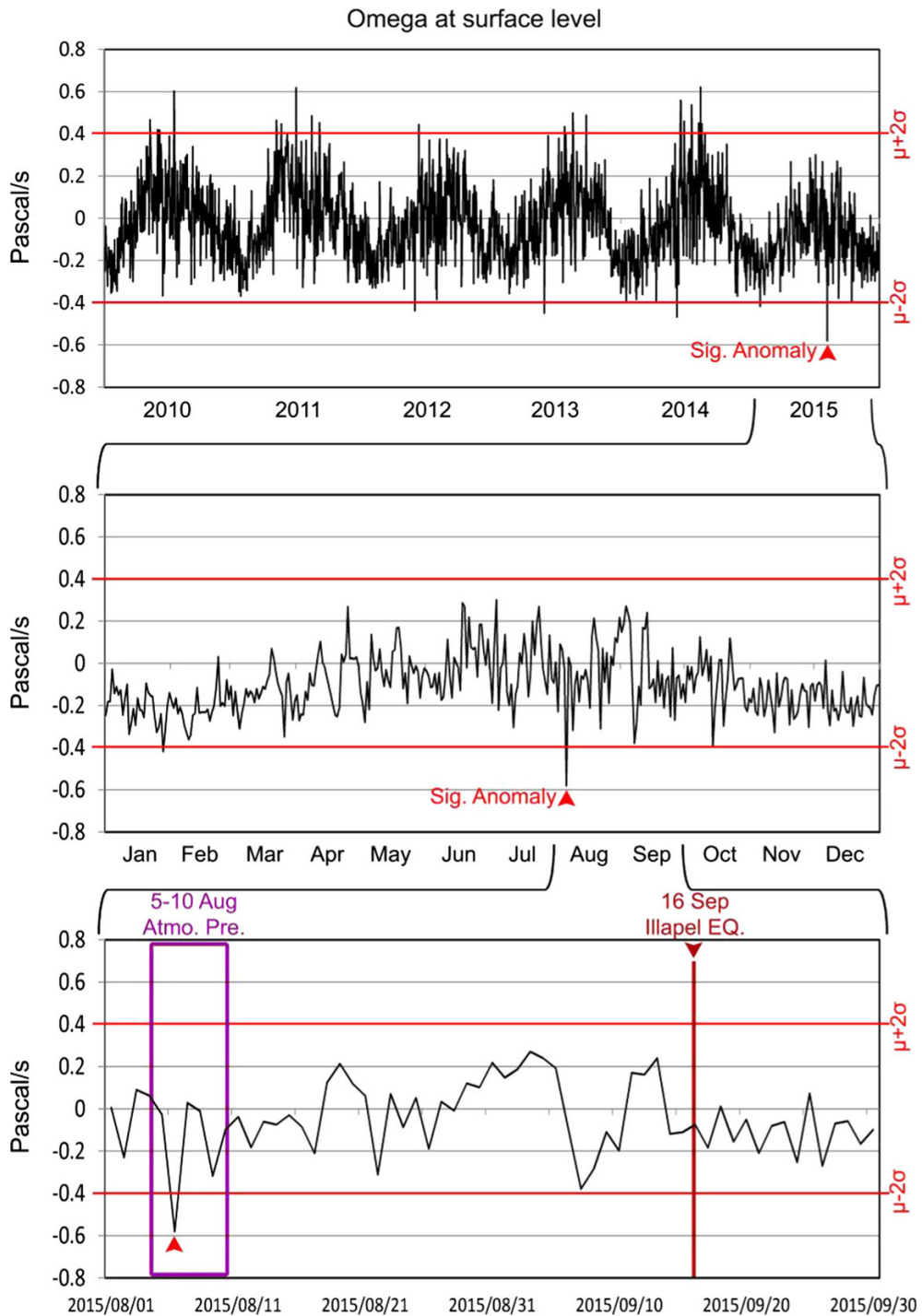


Figure 10

Long-term time series of daily omega index at surface level over the epicentral area and the signals of significant anomalies, extracted from NOAA/PMEL

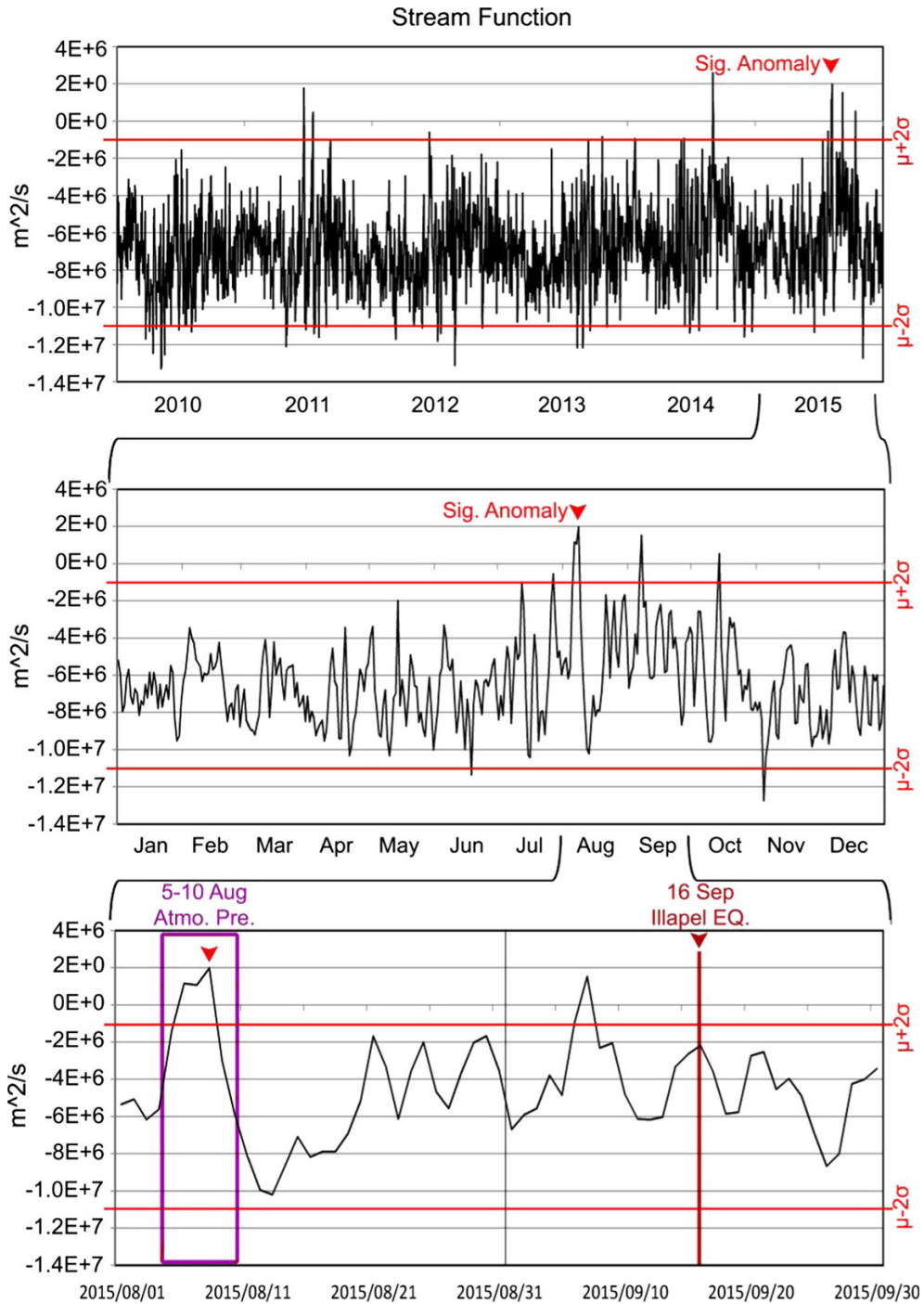


Figure 11

Long-term time series of daily stream function over the epicentral area and the signals of significant anomalies, extracted from NOAA/PMEL

reviewed, including the IRI²⁶ thickness parameter, the altitudes of the ionospheric layers (the minimum virtual height of the F layer, the virtual height at

fMUF-3000, and the maximum height of the F1 layer and the F2 layer), and characteristic frequencies (the minimum frequency for E or F echoes, the

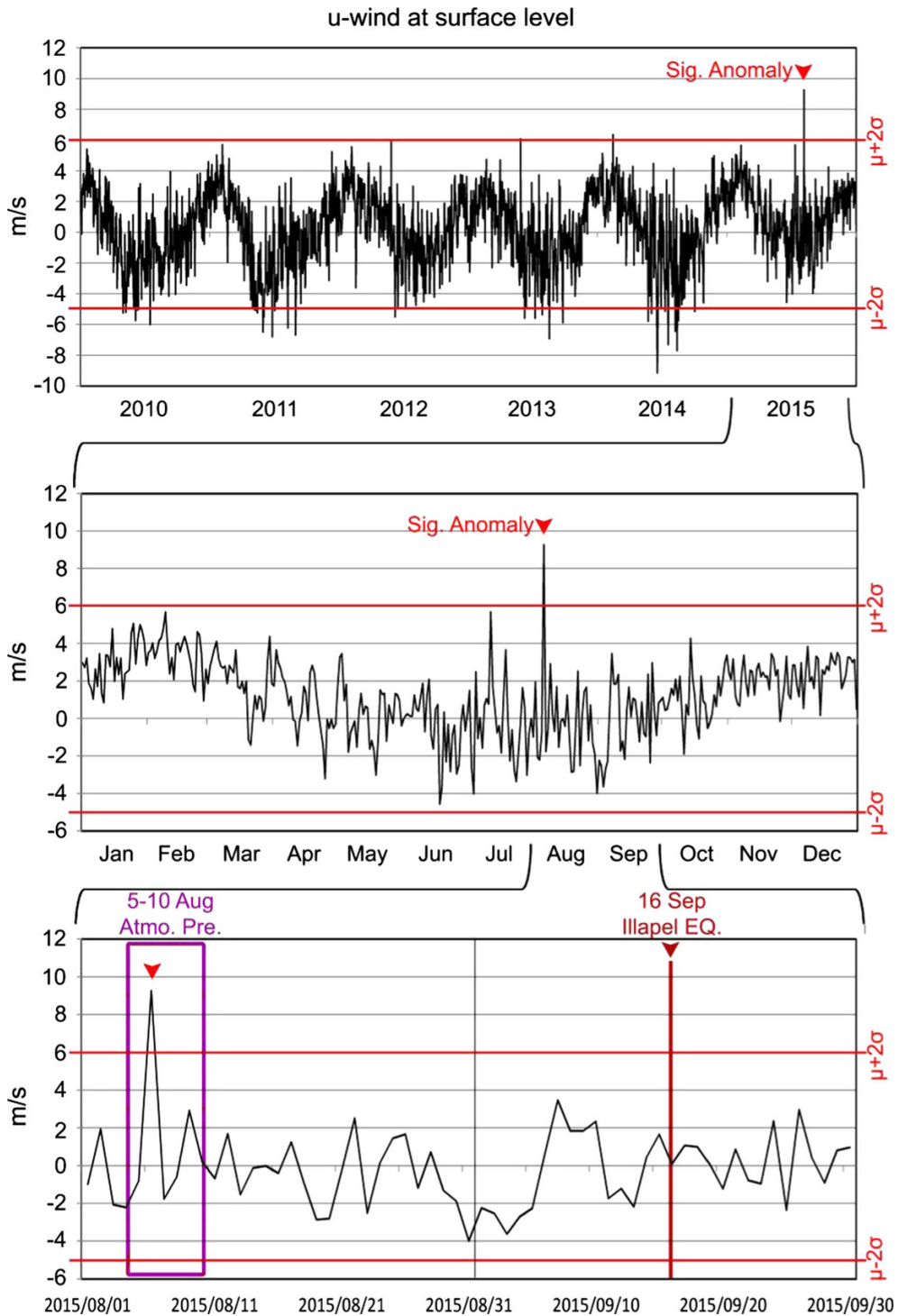


Figure 12

Long-term time series of daily u-wind vector over the epicentral area and the signals of significant anomalies, extracted from NOAA/PMEL

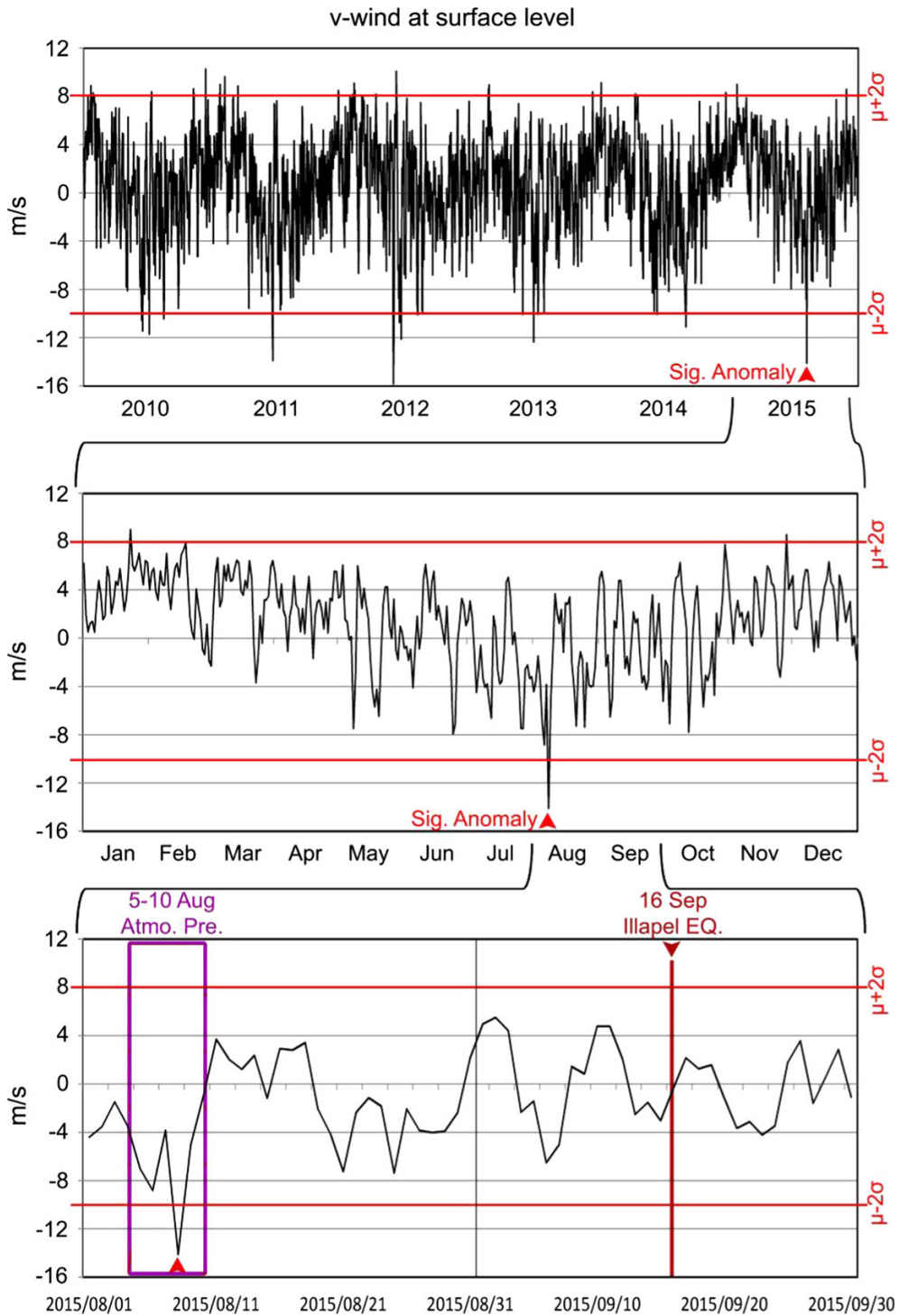


Figure 13

Long-term time series of daily v-wind vector over the epicentral area and the signals of significant anomalies, extracted from NOAA/PMEL

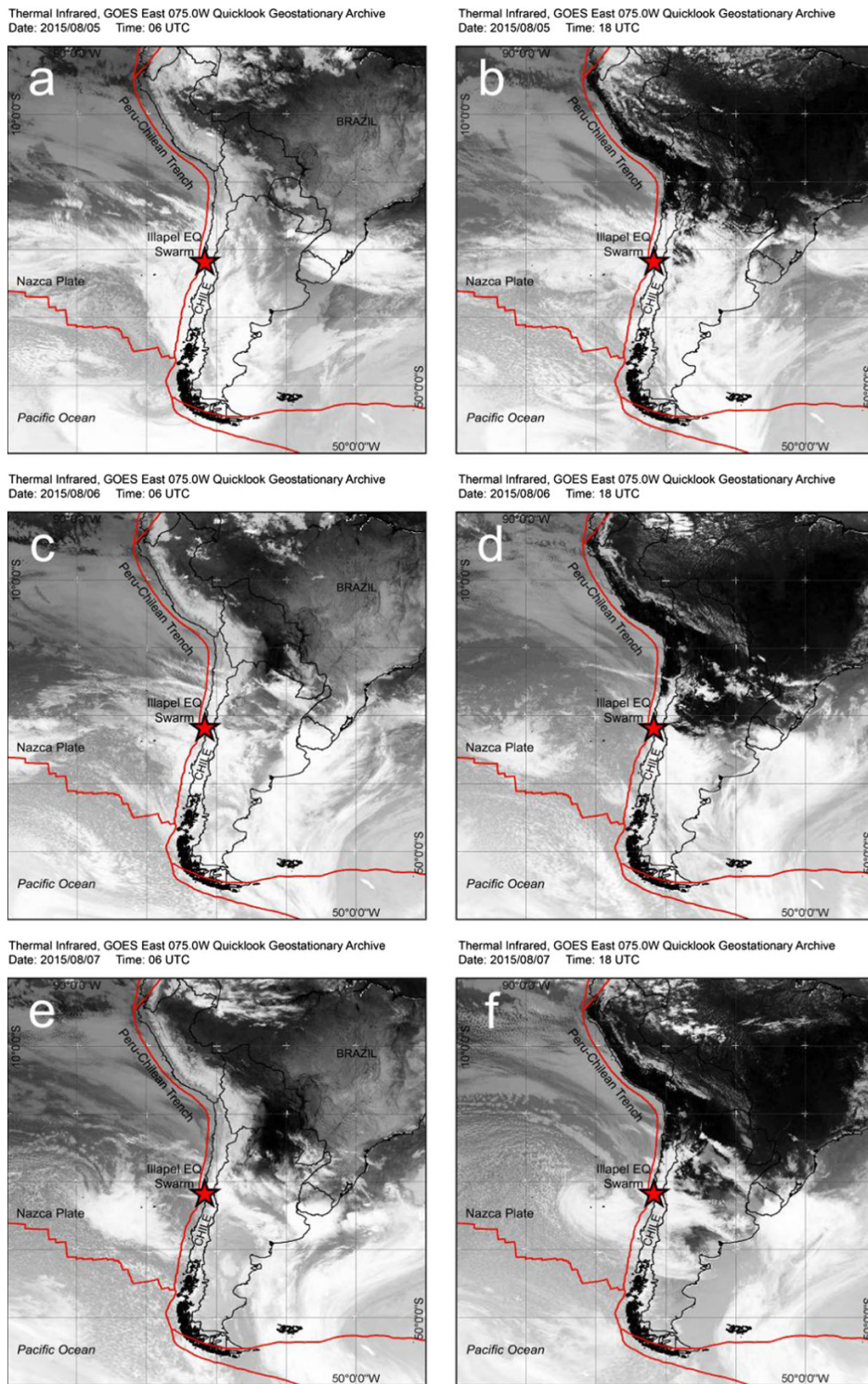


Figure 14
Air turbulence and circulation appeared on thermal infrared images derived from GOES archive on August 5–7, 2015

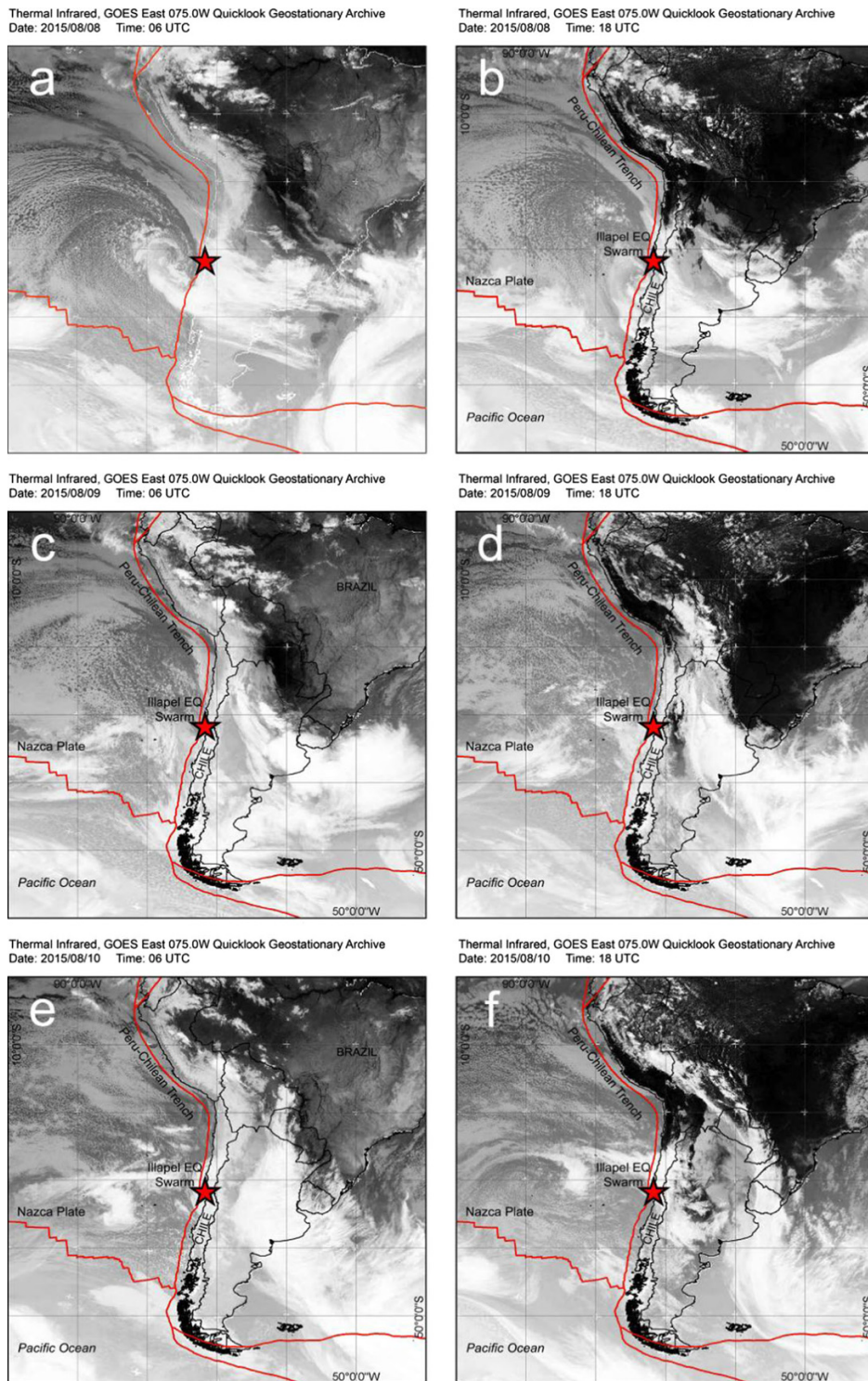


Figure 15
Air turbulence and circulation appeared on thermal infrared images derived from GOES archive on August 8–10, 2015

minimum frequencies of the E-trace and the F-trace, MUF-3000, the obliquity factor, the maximum frequency of the F-trace, and the maximum usable frequency at 3000 km above the earth's surface).

The analysis reveals that during August 15–20, 2015, 5–10 days after the atmospheric anomalies and 25–30 days before the main shock, the IRI thickness parameter abruptly increased and the height of different layers (e.g., minimum vertical height of F-trace) relative to the long-term time series (Figs. 17, 18) also increased. During the same time, the minimum frequency of F-trace abruptly decreased (Fig. 19). Hence, remarkable ionospheric anomalies were recorded about 25–30 days before the September 16, 2015 Mw 8.3 Illapel earthquake. GPS observations, such as daily RINEX²⁷ data, cycle slips, and RMS²⁸ multipath variations, were also considered using the ionosphere-monitoring network at Santiago in Chile. According to these data, an anomaly was also recorded at Santiago on August 15–20, 2015, about 140 km south of the Illapel epicenter (Fig. 20).

Freund (2013) suggested that stress-induced air ionization and formation of positive airborne ions at the ground-to-air interface before major earthquakes, in particular O_2^+ , causes not only an increase of the overall electrical conductivity in the troposphere but leads also to an upward drift of positive airborne ions towards the stratosphere and mesosphere. This in turn will cause a downward motion of the electrons in the ionospheric plasma and, hence, an TEC anomaly. This concept is depicted in Fig. 21 indicating a wide lateral extent of the air ionization process, often inhomogeneous in its intensity, creating a vertical air ion current. This diffuse current is expected to develop magnetohydrodynamic instabilities through coupling to the Earth's magnetic dipole field, breaking up the vertical ion current into regions of higher and lower ion densities, designated as “cells” in Fig. 21. These “cells” would accelerate upward in the Global Electric Field and arriving at the lower edge of the ionosphere with vertical velocities on the order of $20\text{--}30\text{ m s}^{-1}$. The upward motion of these positive charges would induce a downward motion of electrons in the ionospheric plasma, leading to

instabilities at the lower edge of the ionosphere, designated as “ripples” in Fig. 21. The pre-earthquake “turbulences” referred to in papers using data from the DEMETER mission are probably such ripples (Blecki et al. 2011; Zlotnicki et al. 2012). They are the most likely cause for the 2–4 mHz Doppler broadening reported for highly frequency-stabilized 60 kHz radio signals reflected off the ionosphere above earthquake preparation zones (Hayakawa et al. 2012). The observed 2–4 mHz Doppler broadening is consistent with the calculated vertical velocity of $20\text{--}30\text{ m s}^{-1}$ of positive ions, such as O_2^+ , accelerated upward in the Global Electric Field (Freund 2013).

The atmosphere variations prior to the Mw 8.3 Illapel event appear to be causally linked to the ionosphere anomalies, though it should also be noted that, in the case under consideration, the abnormal thunderstorm on August 5–10, 2015 may have contributed to the subsequent ionospheric anomalies. To validate this connection, two-dimensional daily TEC time series was analyzed based on IGS/GIMS data. According to daily TEC in 2015, a significant anomaly was seen on August 14–15, 2015 above Santiago about 140 km south of the Illapel epicenter (Fig. 22). On this basis, the abnormally low values 34–35 days prior to the Mw 8.3 Illapel earthquake coincide with the ionospheric anomalies measured at the Jicamarca station in Lima, Peru, more than 2000 km to the north. During all of 2015 the minimum values of TEC were about 20–25 TECU below the average, but before the Illapel event they deviated by as much as 30–80 TECU. Jianyong et al. (2015) noted that TEC values before earthquakes may decrease and increase in the vicinity of epicenters before earthquakes. Indeed, a number of studies have reported on anomalous reduction in GPS/GIM-TEC several days before major earthquakes (Liu et al. 2004, 2006; Hirooka et al. 2011). A significant decrease of the vertical component of the atmospheric electrical field (VAE) has recorded by Silva et al. (2011) in Portugal before the Sousel earthquake of 2010. However, the aforementioned Fig. 22 reveals a period of declining and increasing TEC values during 2015. In this case, TEC data exhibit typical 1-day, 26.5-day, semi-annual, and annual cycles (Guo et al. 2015). Hence, with respect to the

²⁷ Receiver Independent Exchange.

²⁸ Root mean square.

pre-Illapel data semi-annual and annual TEC cycles may have contributed to the low values in August in addition to any pre-earthquake triggering.

Afraimovich and Astafyeva (2008) reported that the same TEC anomalies as observed prior to earthquakes can occur in response to solar activity and geomagnetic storms. Hence, to distinguish the TEC anomalies from the geomagnetic storms, a diurnal time series of the global Kp index were made based on the SWPC data (Fig. 23). The long-term time series indicated the presence of a geomagnetic storm with Kp index of 6 on August 15–16, 2015, indicative of a moderate geomagnetic storm. However, this perturbation is barely anomalous event compared to the long-term period of a year. The TEC disturbances on August 15–20 appear not be due to solar activities, because geomagnetic storms tend to increase the ionospheric TEC values during the storm days (Chakrabarty et al. 2015) not to decrease. The TEC enhancements associated with geomagnetic storms have been reported from low- to mid-latitudes (Pedatella et al. 2009; Galav et al. 2011; Kumar and Singh 2011).

Several different kinds of earthquake prediction, such as short term, intermediate term, and long term might be possible, each with their own temporal characteristics. A short-term prediction of a few days to weeks would be based on earthquake processes with a short-time scale (Sykes et al. 1999). The spatio-temporal characteristics of atmospheric and ionospheric precursors in this study reveal disturbances within weeks prior to Illapel earthquake. This time window, which is to be characterized as a short term, has analogies to previous electromagnetic and atmospheric studies of earthquake precursory phenomena (Ouzounov et al. 2007; Cicerone et al. 2009; Mansouri Daneshvar et al. 2015). The underlying physical process may be connected to the waxing and waning of tectonic stresses along the fault segment under consideration (Sykes et al. 1999). Episodes of stress-induced massive air ionization at ground level before major earthquakes appear to occur as a result of stress pulses either days or weeks before major earthquakes. However, it should also be remembered that not every build-up of stress will lead to a catastrophic rupture (Heraud 2014). Thus, there may be episodes, where stresses are sufficient

to temporarily induce massive air ionization without being followed by a seismic event.

3.2. Cause for the Pre-Earthquake Anomalies within the Solid Earth

Any earthquake is a mechanical event that begins with tectonic forces subjecting rocks deep in the Earth to increasing levels of mechanical stress and culminates in a catastrophic rupture. If the build-up of mechanical stresses in the Earth's crust is accompanied by atmospheric and ionospheric manifestations, it stands to reason that the mechanical process of stressing the rocks inside the Earth must lead to some ancillary process at the Earth surface, from which the atmospheric and ionospheric anomalies derive. The challenge is to understand how stressing of rocks inside the Earth crust can translate into atmospheric and ionospheric anomalies above the Earth surface.

The most likely coupling mechanism is the stress activation of peroxy defects in the crustal rocks (Freund and Freund 2015a; Scoville et al. 2015). Peroxy defects are ubiquitous in most rocks, though their presence has not yet been widely noted in the geoscience community. They consist of pairs of oxygen anions, for example, $O_3Si-OO-SiO_3$, which have each one electron less than the common oxidation state O^{2-} . Peroxy defects derive from small amounts of solute “water”, typically O_3Si-OH , that become incorporated into the matrix of rock-forming minerals, in particular nominally anhydrous minerals, at the temperature of crystallization from any H_2O -laden magma or during recrystallization in an H_2O -laden high-grade metamorphic environment.

During cooling, after major structural rearrangements involving cation, anion, and vacancy diffusion have slowed down, such that the systems can be considered kinetically frozen, peroxy defects form. The redox conversion of O_3Si-OH pairs to peroxy plus as depicted in Fig. 24a is one reaction that can still take place under thermodynamic non-equilibrium conditions because it requires only minor local shifts in the atomic positions together with a local redistribution of electrons.

The redox conversion is expected to also take place among O_3Si-OH that have segregated to grain boundaries. In this case, peroxy defects will form

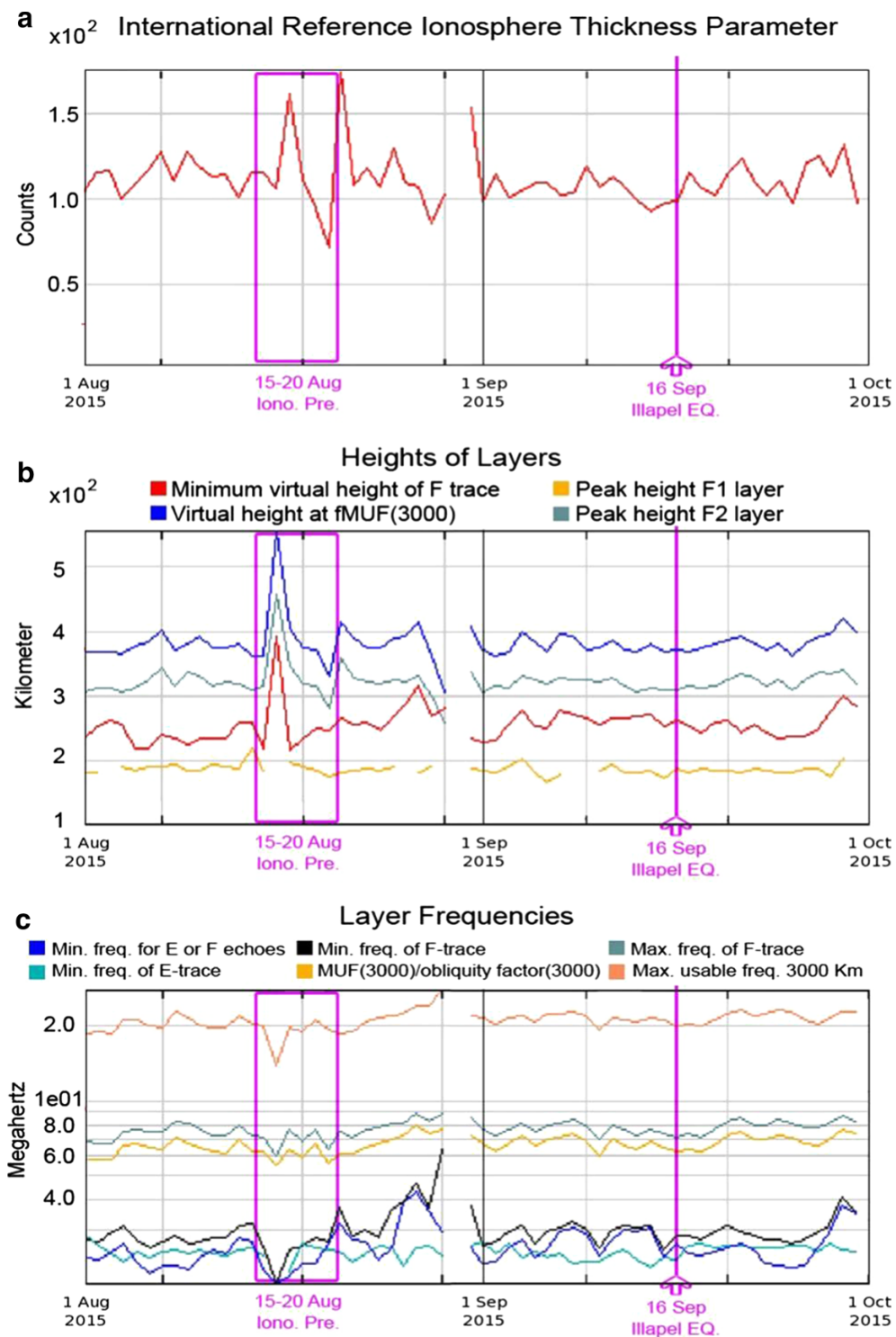


Figure 16

Daily ionospheric variations in Jicamarca station on August and September 2015, including **a** IRI thickness parameter, **b** heights of layer, and **c** layer frequencies extracted from NOAA/SPIDR

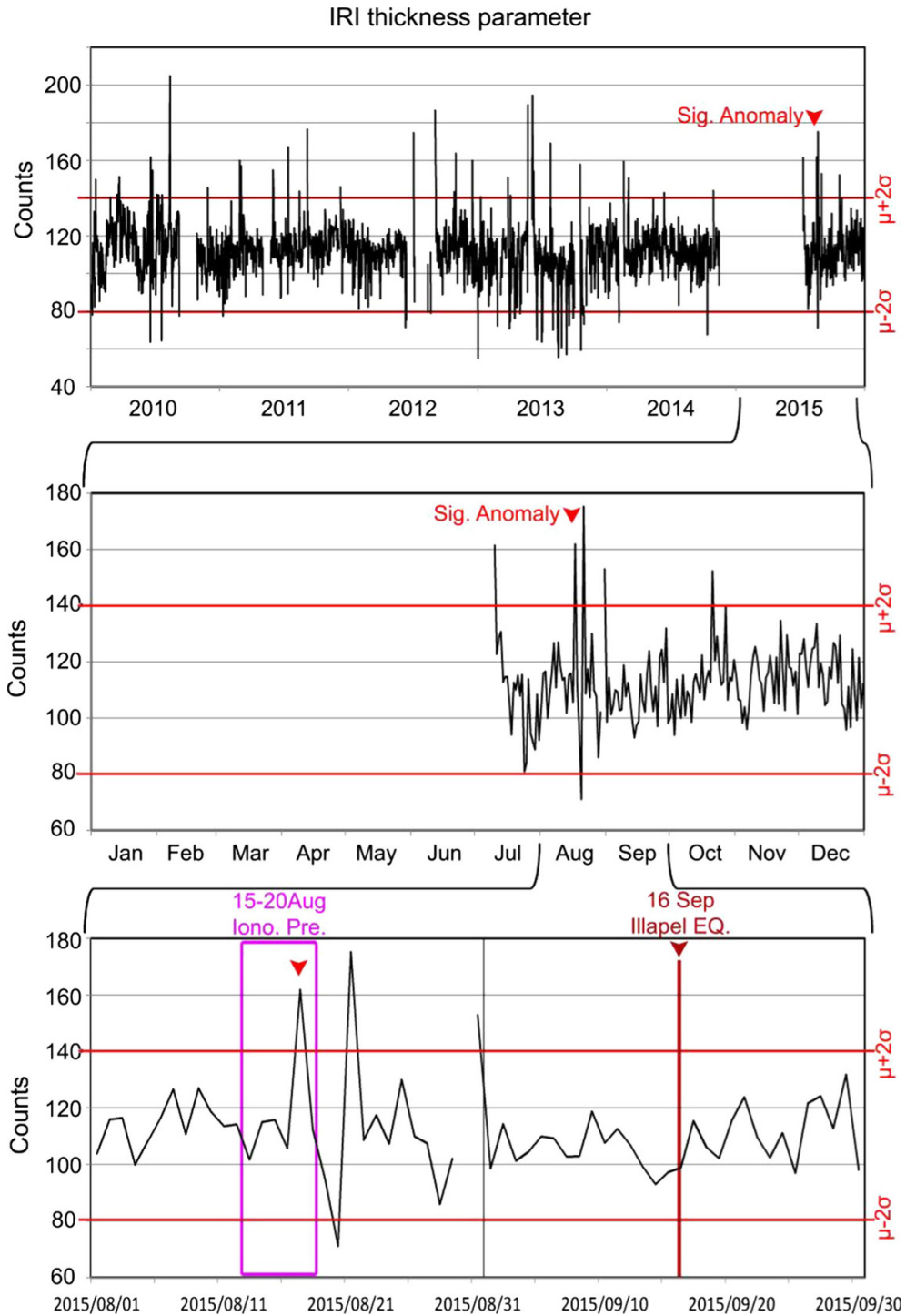


Figure 17

Long-term time series of IRI thickness parameter in Jicamarca station and the signals of significant anomalies, extracted from NOAA/SPIDR

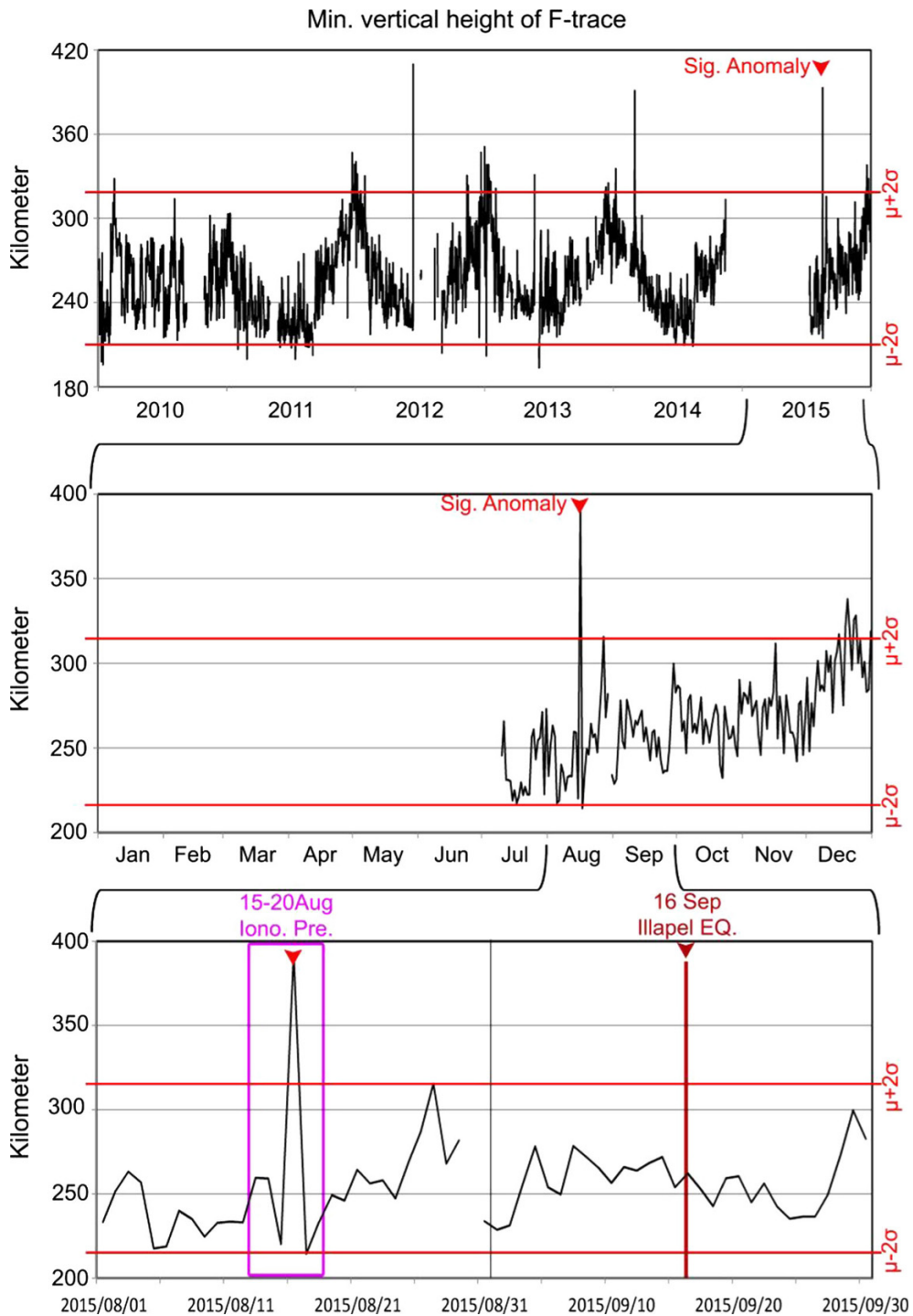


Figure 18

Long-term time series of minimum vertical height of F-trace in Jicamarca station and the signals of significant anomalies, extracted from NOAA/SPIDR

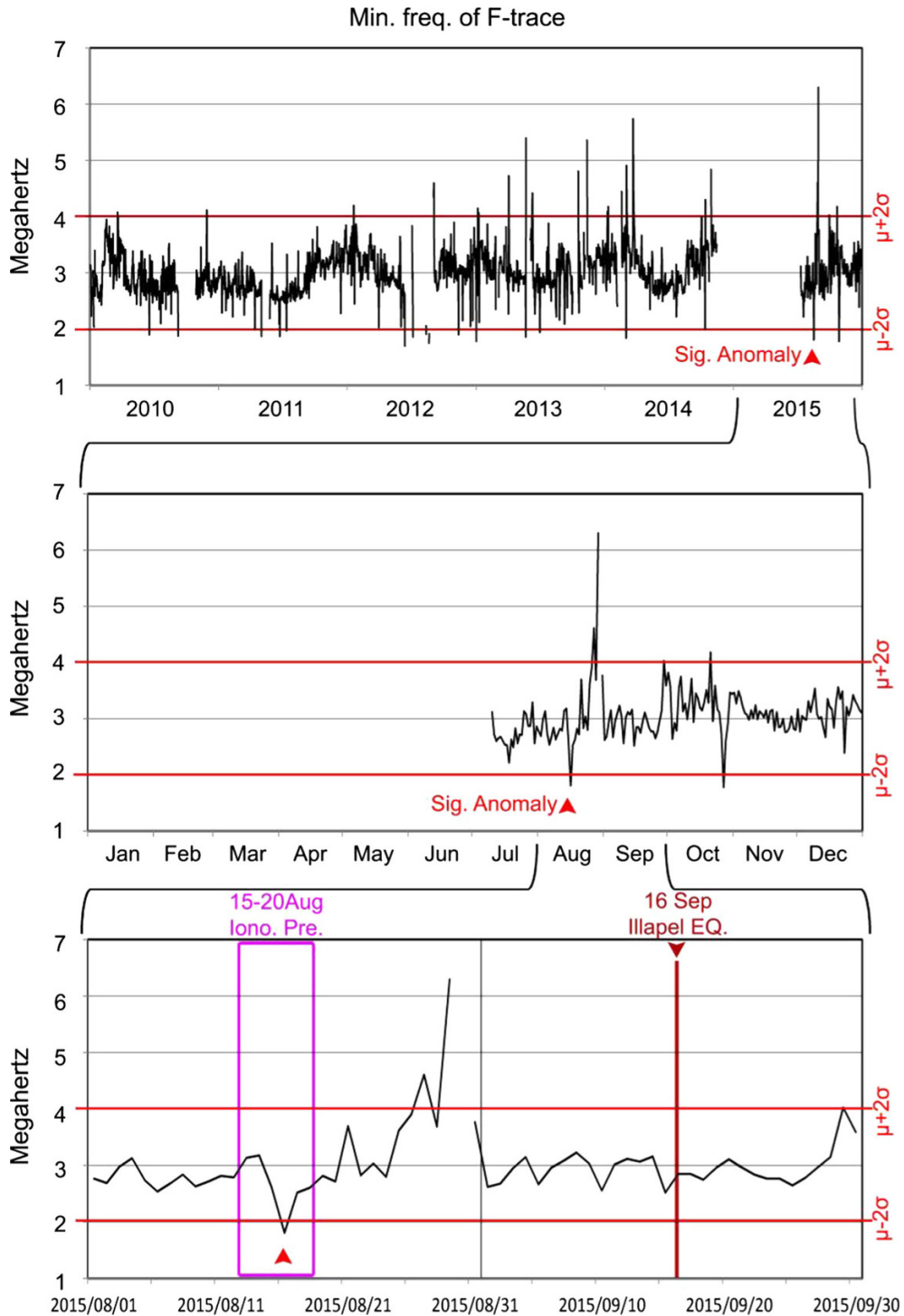


Figure 19

Long-term time series of the minimum frequency of the F-trace at the Jicamarca station and the signals of significant anomalies, extracted from NOAA/SPIDR

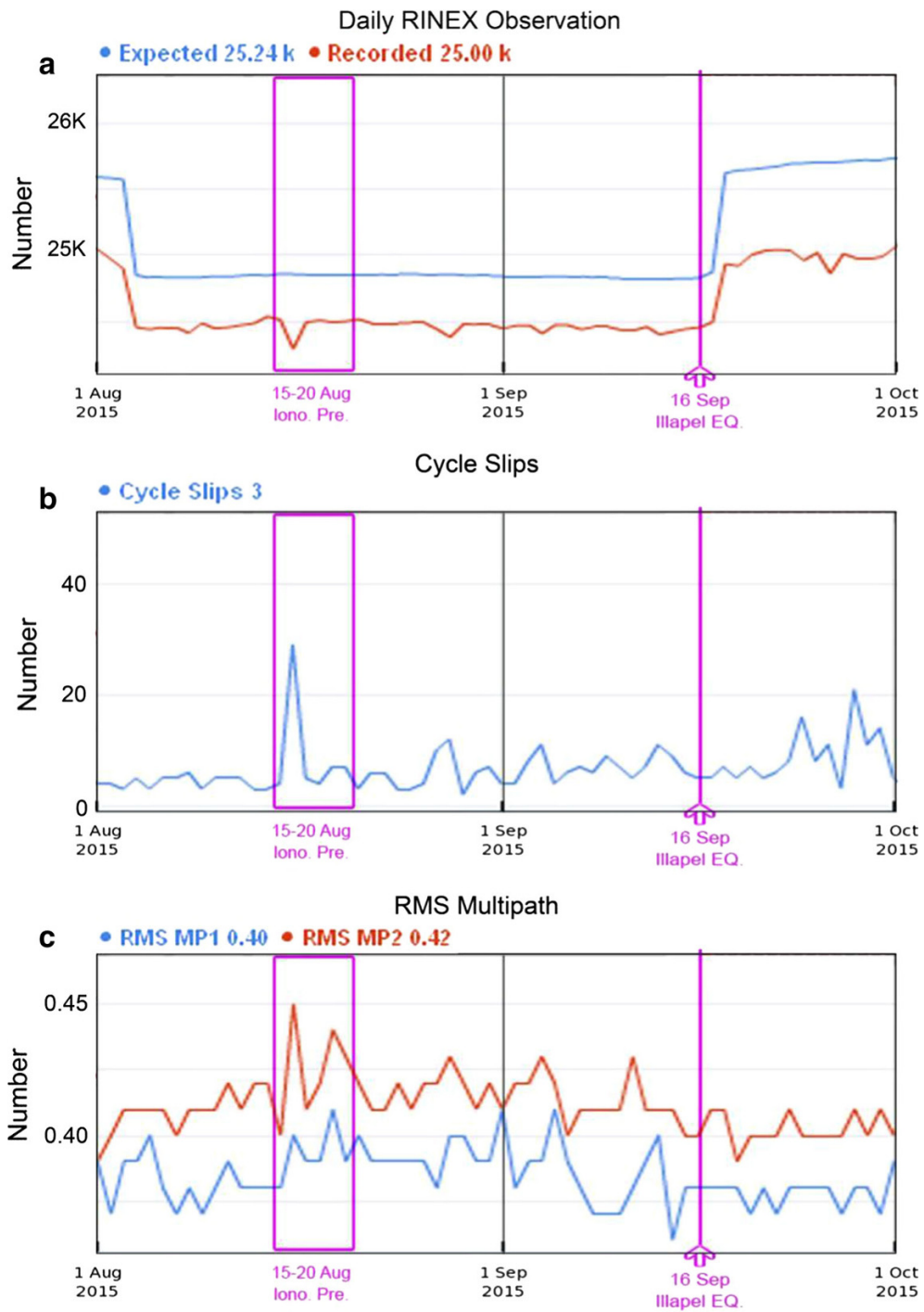


Figure 20

Quality of data observations obtained at the Santiago station on August and September 2015, including **a** RINEX observation, **b** cycle slips, and **c** RMS multipath extracted from IGS/GPS

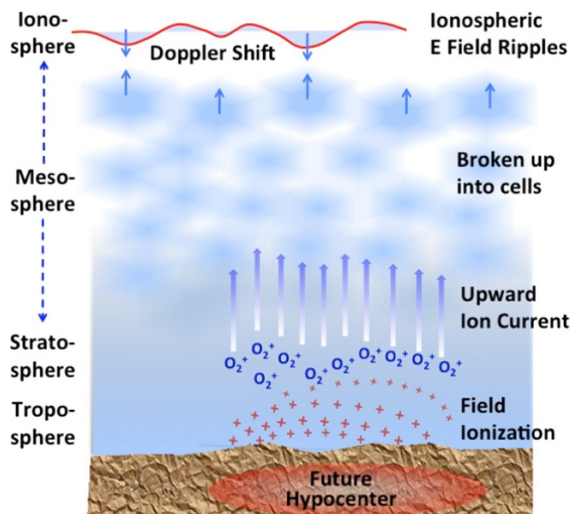


Figure 21

Schematic representation of processes initiated by air ionization at ground level as a result of the stress activation of peroxy defects in the hypocentral volume deep in the Earth's crust and flow of positive hole charge carriers to the Earth surface. The positive airborne ions are expected to rise through the atmospheric column due to the thermal updraft caused by the release of latent heat during condensation of moisture and due to the upward acceleration in the prevailing Global Electric Field. The diffuse vertical ion current is expected to develop instabilities, breaking up into cells, which continue to drift towards the ionosphere, causing a response from the electrons in the ionospheric plasma

along and across grain–grain contacts, making them especially susceptible to activation by mechanical stresses that cause ever so slight displacements of mineral grains relative to each other (Scoville et al. 2015). Deformation of the Si–OO–Si bonds then generates electron–hole pairs, as illustrated in Fig. 24b. The electrons (e^-) become trapped in the broken peroxy bonds, whereas the holes (h^*) turn into highly mobile electronic charge carriers, called “positive holes” (Freund and Freund 2015a).

Positive holes have the remarkable ability to flow out of the stressed rock volume into and through the surrounding less stressed and unstressed rocks, traveling fast and far. When they reach the Earth's surface, they accumulate over a wide area, setting up microscopic but steep electric fields at the ground-to-air interface (Freund et al. 2009; Freund 2013). As the tectonic stresses deep below increase during the period of earthquake preparation, the number of positive holes arriving at the ground-to-air interfaces will increase. When their number density exceeds

some threshold value, the local electric fields become strong enough to field-ionize gas molecules. This effect has been predicted (King and Freund 1984), has been demonstrated in laboratory experiments (Freund et al. 2009), and confirmed in the field (Bleier et al. 2009). Of all major air constituents, O_2 has the lowest ionization potential, 12.07 eV, followed by H_2O with 12.61 eV (Biemont et al. 1999).

The field ionization at the ground-to-air interface is a highly dynamic process. It depends on how many positive holes arrive at the surface. They recombine to form peroxy bonds, an exothermal reaction, which leads to vibrationally highly excited states that de-excite radiatively, emitting infrared photons in the thermal infrared band, 7–14 μm (Freund et al. 2007). However, for each peroxy bond forming at the ground-to-air interface, two positive charges are deposited, contributing to the build-up of the positive surface charge and its associated electric field. This surface charge tends to block the influx of further positive holes to the surface from below, effectively shutting off the infrared emission.

At the same time, however, when the positive surface charge reaches values sufficiently high values, air ionization sets in. The transfer of electrons from air molecules onto the surface reduces the positive surface charge, allowing the next wave of positive holes to reach the surface and to start the infrared emission process anew. As a result, bursts of infrared photons emitted from the surface will alternate with bursts of positive airborne ions formed at the ground-to-air interface.

This highly dynamic behavior has been independently observed for the thermal infrared emission, both in the laboratory (Freund et al. 2007) and the field (Piroddi and Ranieri 2012), and for the air ionization laboratory experiments (Freund et al. 2009) and for field observations (Bleier et al. 2009).

Figure 25a shows the positive air ionization prior to October 31, 2007 3:04 UT M 5.6 Alum Rock earthquake in California, recorded by a QuakeFinder station fortuitously located only 2 km from the epicenter (Bleier et al. 2009). Up to late October 29th, 27 h before the event, the air ionization level was close to the “fair weather value”, ~ 200 ions cm^{-3} (Rycroft et al. 2008). Then, about 21 h before the main shock, massive air ionization started, which

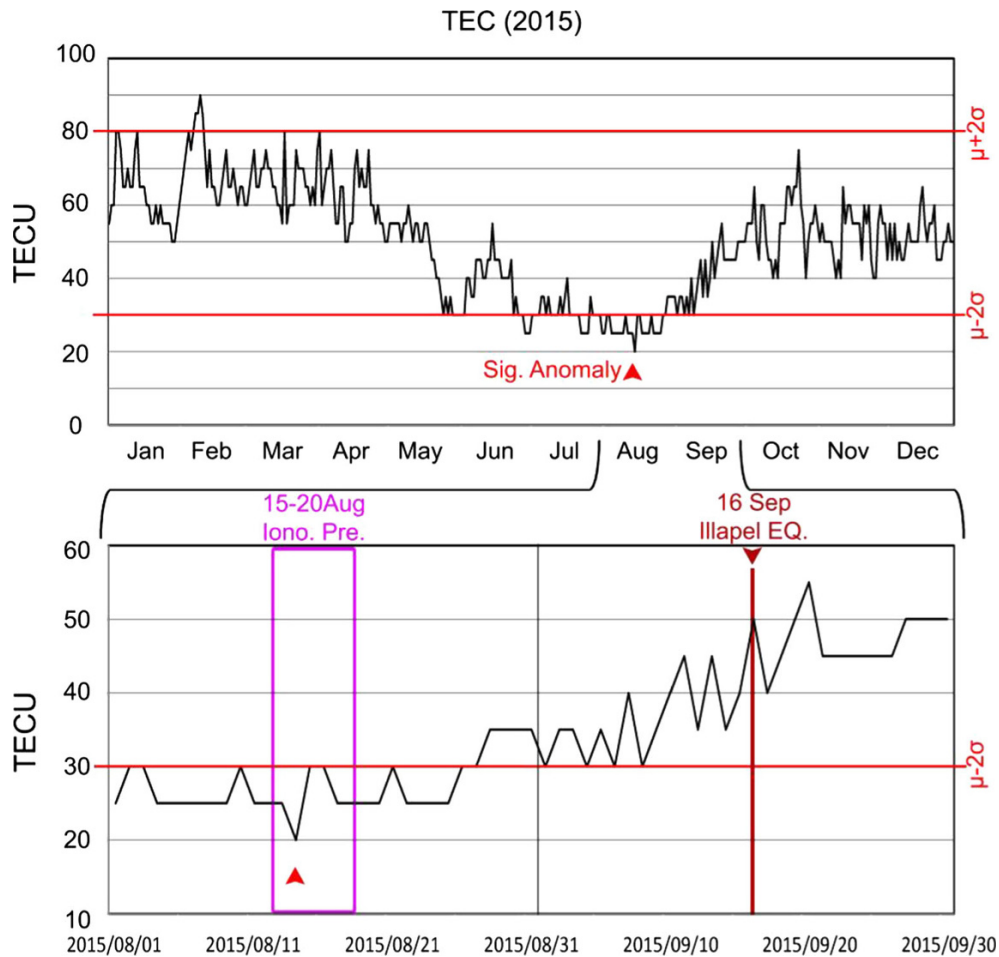


Figure 22

Long-term time series of maximum TEC in vicinity of the earthquake epicenter and the signals of significant anomalies, extracted from IGS/GIMs

lasted about 14 h. It saturated the available sensor, probably reaching values on the order of $20,000 \text{ ions cm}^{-3}$ as has been observed at other locations (Yada and Saito 2012).

The onset of the air ionization was marked by discrete pulses. Figure 25b shows a series of such pulses, arriving in ~ 5 min intervals, indicating a coupled process at the ground-to-air interface, where the air ionization took place. Due to the Coulomb repulsion between the positively charged air ions, the ion ionization pulses are expected to create air pressure pulses, which would propagate outward and upward leading to ionospheric perturbations similar to Atmospheric Gravity Waves (AGW) normally generated only co-seismically, i.e., during earthquakes, as the result of vertical motion of the

Earth surface (Garcia et al. 2005; Lizunov and Hayakawa 2004; Rozhnoi et al. 2007). Notably, AGWs have been reported at numerous occasions as pre-earthquake phenomena occurring without the Earth surface acting as a moving membrane (Hayakawa et al. 2011; Hegai et al. 2006; Klimenko et al. 2011)—an observation that is consistent with massive pre-earthquake positive air ionization at the Earth surface as reported here. A corollary of the production of air ions of one sign would be the generation of strong vertical winds due to the Coulomb explosion of the heavily ion-laden air, possibly up to the point of initiating atmospheric anomalies described here as a strong cyclone that developed above the epicentral region as documented in Figs. 6, 7, 8, 9, 10, 11, 12, and 13.

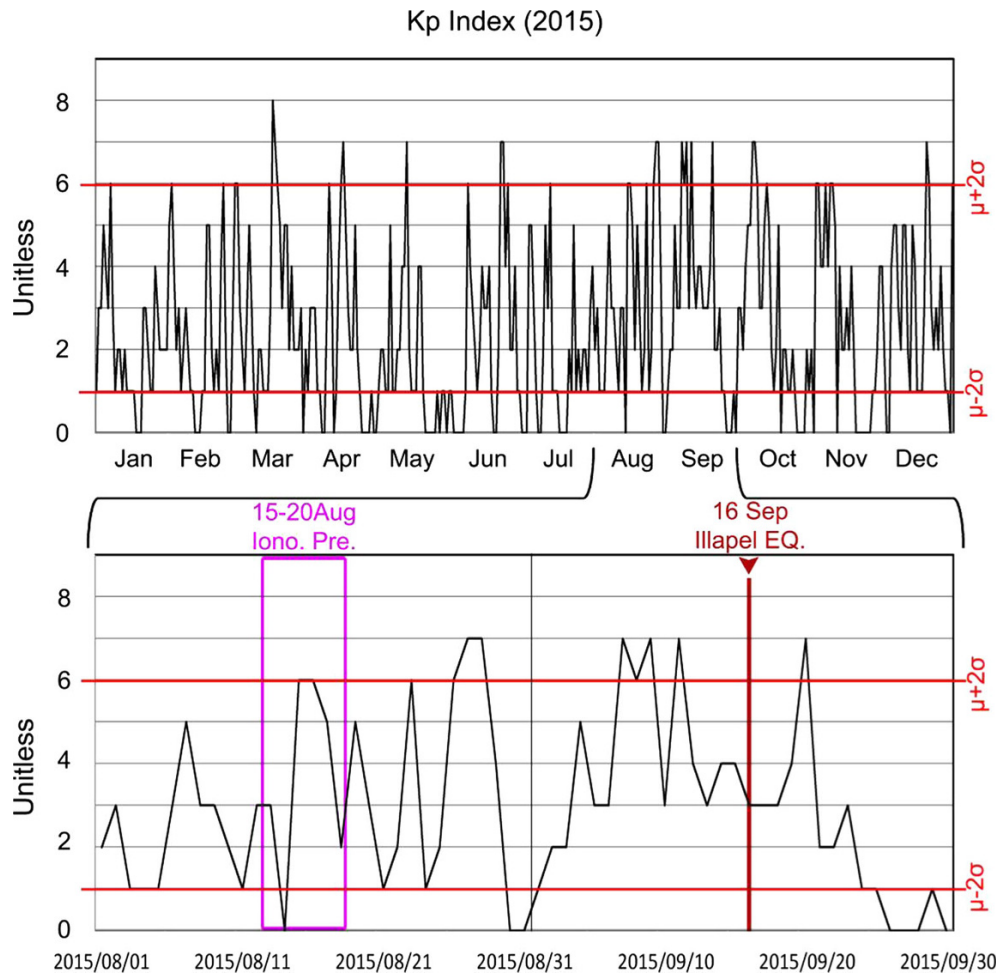


Figure 23
Long-term time series of global Kp index, extracted from NOAA/SWPC

Theory predicts and laboratory experiments have confirmed that further influx of positive holes to the ground-to-air at the Earth surface interface must lead still higher electric fields. Eventually, these electric fields reach values high enough to accelerate adventitious free electrons, which are always available in the air due to cosmic rays and radioactive decay, to kinetic energies sufficient to impact ionize gas neutrals. This is the triggering process of corona discharges, which produce small light blips and an overabundance of free electrons that attach themselves to neutral gas molecules generating negative airborne ions (Freund et al. 2009).

Laboratory experiments have indeed demonstrated that, when the transition occurs from field

ionization to corona discharges, the sign of the surface charge abruptly changes from positive to negative (Freund et al. 2009). Simultaneously, ozone is produced as by-product of the corona discharges. The observed increase in cloud cover prior to the Illapel earthquake as documented in Fig. 2 and increase of the tropospheric ozone concentration as documented in Fig. 3 are consistent with this overall concept of the processes that result from the stress activation of large numbers of positive hole charge carriers in and around the hypocentral volume and their flow to the Earth surface.

Further studies about the global linkage between the various pre-earthquake phenomena and future seismic events can be considered under NASA



Figure 24

a Schematic representation of the dissolution of H₂O into the matrix of silicate minerals and the redox conversion of hydroxyl pairs to a peroxy defect plus molecular H₂. **b** Schematic representation of the break-up of the peroxy bond. From left to right: application of stress changes the Si-OO-Si bond angle; decoupling of the Si-OO-Si bond and transfer of an electron from a neighboring O²⁻; and trapping of the electron in the broken peroxy bond and formation of a hole state, which represents a highly mobile positive hole charge carrier

mission support services at the agency's Ames Research Center in Moffett Field, California (<https://www.nasa.gov/press/2014/july/nasa-selects-contract-for-mission-support-services-at-ames>).

4. Conclusion

In this paper, the temporal and spatial evolutions of a range of distinct atmospheric and ionospheric variations have been documented, as they became discernable in multisource remote-sensing data prior to the Chilean Mw 8.3 Illapel earthquake of September 16, 2015. Evidence was found for pre-earthquake co-occurring anomalous variations in atmospheric parameters, such as cloud coverage and daily precipitation, sea-level air pressure and geopotential height at 1000 and 500 hPa, daily stream function and v-wind and u-wind vectors, and trace gas column thickness for O₃ and SO₂, within the time window around August 5–10, 2015, some 25–30 days before the seismic event, plus the co-appearance of an abnormal cyclone over the epicentral region. At the same time, anomalous variations were also noted in ionospheric parameters recorded in Peru, more than 2000 km to the North of the Illapel epicenter, such as the height of the F layer, and in the Total Electron

Content (TEC) over the epicentral area in the August 15–20, 2015 time window, 5–10 days after the main atmospheric anomalies. The ionospheric variations seem not to be due to geomagnetic storm activity as indicated by the Kp values remaining >6 during the period of interest.

While the temporal separation of the atmospheric anomalies before the Mw 8.3 Illapel earthquake is somewhat unusual—35 to 40 days—the co-occurrence of the range of observables is consistent with the processes that take place at the ground-to-air interface as a result of stress activation of peroxy defects in the rocks in the hypocentral volume: the outflow of highly mobile positive hole charge carriers from the source volume, their travel through the rock column, and their accumulation at the ground-to-air interface. Most significant for the topic of this paper is that fact that, as positive holes accumulate at the Earth surface, they build up surface charges and associated electric fields, microscopic but strong enough to: (1) massively field-ionize gas molecules, mostly O₂ to produce massive amounts of O₂⁺ ions, which rise through the atmospheric column causing a variety of secondary processes on the way and (2) trigger corona discharges, which produce an abundance of free electrons, negative airborne ions, and ozone.

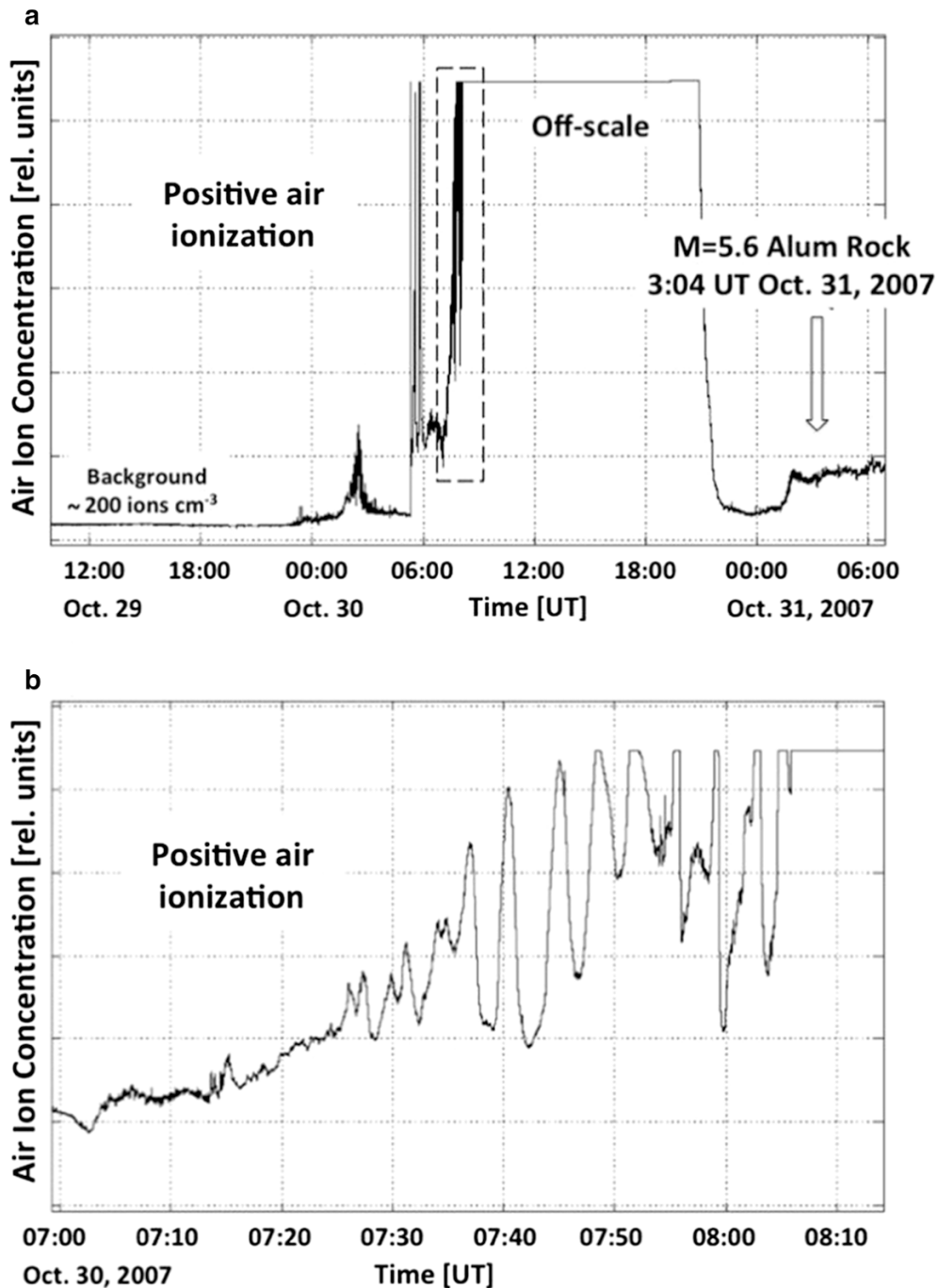


Figure 25

Episode of intense positive air ionization prior to the M 5.6 Alum Rock earthquake of October 31, 2007, California, USA. **a** Last 27 h before the main shock. **b** Discrete air ionization pulses during the onset of main ionization event (*dashed box*)

Understanding the sequence of reactions inside the Earth's crust and at the ground-to-air interface provides additional information not previously

available result from the stress activation of large numbers of positive hole charge carriers about the causal and temporal linkage between the various pre-

earthquake phenomena and the future seismic event. This might be beneficial for developing earthquake forecasting programs for the highly active subduction zone of the Nazca plate beneath the South American continent along the Peru-Chilean coast, which has historically generated many large to very large earthquakes.

Acknowledgments

We wish to acknowledge the NASA and NOAA online data centers for global transmission of reanalysis data. Friedemann T. Freund acknowledges support from the NASA ESI grant NNX12AL71G through the San Jose State University Foundation.

REFERENCES

- Afraimovich, E. L., & Astafyeva, E. I. (2008). TEC anomalies—local TEC changes prior to earthquakes or TEC response to solar and geomagnetic activity changes? *Earth Planets and Space*, 60(9), 961–966.
- Aleksandrov, N. L., Bazelyan, E. M., Carpenter, R. B., Drabkin, M. M., & Raizer, Y. P. (2001). The effect of coronae on leader initiation and development under thunderstorm conditions and in long air gaps. *Journal of Physics D Applied Physics*, 34, 3256–3266.
- Alvan, H. V., Mansor, S., Omar, H., & Azad, F. H. (2014). Precursory signals associated with the 2010 M8.8 Bio-Bio earthquake (Chile) and the 2010 M7.2 Baja California earthquake (Mexico). *Arabian Journal of Geosciences*, 7(11), 4889–4897.
- Biemont, E., Fremat, Y., & Quinet, P. (1999). Ionization potentials of atoms and ions from lithium to tin ($z = 5-50$). *Atomic Data and Nuclear Data Tables*, 71, 117–146.
- Blakeslee, R. J., Christian, H. J., & Vonnegut, B. (1989). Electrical measurements over thunderstorms. *Journal of Geophysical Research*, 95(D11), 135–113, 140.
- Blecki, J., Parrot, M., & Wronowski, R. (2011). Plasma turbulence in the ionosphere prior to earthquakes, some remarks on the DEMETER registrations. *Journal of Asian Earth Sciences*, 41, 450–458.
- Bleier, T., Dunson, C., Maniscalco, M., Bryant, N., Bamberg, R., & Freund, F. T. (2009). Investigation of ULF magnetic pulsations, air conductivity changes, and infra red signatures associated with the 30 October 2007 Alum Rock M5.4 earthquake. *Natural Hazards and Earth Systems Sciences*, 9, 585–603.
- Chakraborty, M., Kumar, S., De Kumar, B., & Guha, A. (2015). Effects of geomagnetic storm on low latitude ionospheric total electron content: a case study from Indian sector. *Journal of Earth System Science*, 124(5), 1115–1126.
- Cicerone, R. D., Ebel, J. E., & Britton, J. (2009). A systematic compilation of earthquake precursors. *Tectonophysics*, 476(3–4), 371–396.
- Dobrovolsky, I. P., Zubkov, S. I., & Myachkin, V. I. (1979). Estimation of the size of earthquake preparation zones. *Pure and Applied Geophysics*, 117, 1025–1044.
- Freund, F. T. (2003). Rocks that crackle and sparkle and glow: strange pre-earthquake phenomena. *Journal of Scientific Exploration*, 17(1), 37–71.
- Freund, F. T. (2011). Pre-earthquake signals: underlying physical processes. *Journal of Asian Earth Sciences*, 41, 383–400.
- Freund, F. T. (2013). Earthquake forewarning—a multidisciplinary challenge from the ground up to space. *Acta Geophysica*, 61(4), 775–807.
- Freund, F.T. & Freund M.M. (2015a). Paradox of peroxy defects and positive holes in rocks part I: effect of temperature. *Journal of Asian Earth Sciences*, 114(2), 3730150383.
- Freund, F. T., & Freund, M. M. (2015b). From where did the water come that filled the earth's oceans? a widely overlooked redox reaction. *American Journal of Analytical Chemistry*, 6, 342–349.
- Freund, F. T., Kulahci, I. G., Cyr, G., Ling, J., Winnick, M., Tregloan-Reed, J., et al. (2009). Air ionization at rock surfaces and pre-earthquake signals. *Journal of Atmospheric and Solar Terrestrial Physics*, 71(17-18), 1824–1834.
- Freund, F. T., Takeuchi, A., Lau, B. W. S., Al-Manaseer, A., Fu, C. C., Bryant, N. A., et al. (2007). Stimulated thermal IR emission from rocks: assessing a stress indicator. *eEarth*, 2, 1–10.
- Galav, P., Sharma, S., & Pandey, R. (2011). Study of simultaneous penetration of electric fields and variation of total electron content in the day and night sectors during the geomagnetic storm of 23 May 2002. *Journal of Geophysical Research Space Physics*. doi:10.1029/2011JA017002.
- Galvan, D. A., Komjathy, A., Hickey, M. P., & Mannucci, A. J. (2011). The 2009 Samoa and 2010 Chile tsunamis as observed in the ionosphere using GPS total electron content. *Journal of Geophysical Research*. doi:10.1029/2010JA016204.
- Ganguly, N. D. (2016). Atmospheric changes observed during April 2015 Nepal earthquake. *Journal of Atmospheric and Solar Terrestrial Physics*, 140, 16–22.
- Garcia, R., Crespon, F., Ducic, V., & Lognonné, P. (2005). Three-dimensional ionospheric tomography of post-seismic perturbations produced by the Denali earthquake from GPS data. *Geophysical Journal International*, 163, 1049–1064.
- Guo, J., Li, W., Liu, X., Kong, Q., Zhao, C., & Guo, B. (2015). Temporal-Spatial Variation of Global GPS-Derived Total Electron Content, 1999–2013. *PLoS One*, 10(7), e0133378.
- Gusman, A. R., Murotani, S., Satake, K., Heidarzadeh, M., Gunawan, E., Watada, S., et al. (2015). Fault slip distribution of the 2014 Iquique, Chile, earthquake estimated from ocean-wide tsunami waveforms and GPS data. *Geophysical Research Letters*, 42(4), 1053–1060.
- Hayakawa, M., Kasahara, T. E. Y., Hobara, Y., & Asai, S. (2012). The observation of Doppler shifts of subionospheric LF signal in possible association with earthquakes. *Journal of Geophysical Researches*, 117, A09304.
- Hayakawa, M., Kasahara, Y., Nakamura, T., Hobara, Y., Rozhnoi, A., Solovieva, M., et al. (2011). Atmospheric gravity waves as a possible candidate for seismo-ionospheric perturbations. *Journal of Atmospheric Electricity*, 31(2), 129–140.
- Hegai, V. V., Kim, V. P., & Liu, J. Y. (2006). The ionospheric effect of atmospheric gravity waves excited prior to strong earthquake. *Advances in Space Research*, 37, 653–659.

- Heraud, J. (2014). Pre-earthquake signals at the ground level. In F. Freund & S. Langhoff (Eds.), *Universe of Scales: from nanotechnology to cosmology* (pp. 133–157). Berlin: Springer.
- Hirooka, S., Hattori, K., Nishihashi, M., & Takeda, T. (2011). Neural network based tomographic approach to detect earthquake-related ionospheric anomalies. *Natural Hazards and Earth System Sciences*, *11*, 2341–2353.
- Ho, Y. Y., Jhuang, H. K., Su, Y. C., & Liu, J. Y. (2013a). Seismo-ionospheric anomalies in total electron content of the GIM and electron density of DEMETER before the 27 February 2010 M8.8 Chile earthquake. *Advances in Space Research*, *51*(12), 2309–2315.
- Ho, Y. Y., Liu, J. Y., Parrot, M., & Pinçon, J. L. (2013b). Temporal and spatial analyses on seismo-electric anomalies associated with the 27 February 2010 M = 8.8 Chile earthquake observed by DEMETER satellite. *Natural Hazards and Earth System Sciences*, *13*(12), 3281–3289.
- Hsu, S. C., Huang, Y. T., Huang, J. C., Tu, J. Y., Engling, G., Lin, C. Y., et al. (2010). Evaluating real-time air-quality data as earthquake indicator. *Science of the Total Environment*, *408*(11), 2299–2304.
- Jianyong, L., Jianyong, M., Xinzhaoy, Y., Rui, Z., Hongbo, S., & Yufei, H. (2015). Ionospheric total electron content disturbance associated with May 12, 2008. *Wenchuan Earthquake. Geodesy and Geodynamics*, *6*(2), 126–134.
- King, B. V., & Freund, F. T. (1984). Surface charges and subsurface space charge distribution in magnesium oxide containing dissolved traces of water. *Physical Review B*, *29*, 5814–5824.
- Klimenko, M. V., Klimenko, V. V., Zakharenkova, I. E., Pulinets, S. A., Zhao, B., & Tsidilina, M. N. (2011). Formation mechanism of great positive TEC disturbances prior to Wenchuan earthquake on May 12, 2008. *Advances in Space Research*, *48*, 488–499.
- Kumar, S., & Singh, A. K. (2011). GPS derived ionospheric TEC response to geomagnetic storm on 24 August 2005 at Indian low latitude stations. *Advances in Space Research*, *47*, 710–717.
- Liu, J. Y., Chen, Y. I., Chuo, Y. J., & Chen, C. S. (2006). A statistical investigation of pre-earthquake ionospheric anomaly. *Journal of Geophysical Research Space Physics*. doi:10.1029/2005JA011333.
- Liu, J. Y., Chuo, Y. J., Shan, S. J., Tsai, Y. B., Chen, Y. I., Pulinets, S. A., et al. (2004). Pre-earthquake ionospheric anomalies registered by continuous GPS TEC measurements. *Annales Geophysicae*, *22*, 1585–1593.
- Lizunov, G., & Hayakawa, M. (2004). Atmospheric gravity waves and their role in the lithosphere-troposphere-ionosphere interaction. *IEEJ Transactions on Fundamentals and Materials A*, *124*, 12.
- Mansouri Daneshvar, Tavousi, T., & Khosravi, M. (2014). Synoptic detection of the short-term atmospheric precursors prior to a major earthquake in the Middle East, North Saravan M 7.8 earthquake, SE Iran. *Air Quality and Atmosphere Health*, *7*(1), 29–39.
- Mansouri Daneshvar, M. R., Tavousi, T., & Khosravi, M. (2015). Atmospheric blocking anomalies as the synoptic precursors prior to the induced earthquakes; a new climatic conceptual model. *International Journal of Environmental Science and Technology*, *12*(5), 1705–1718.
- Mukhtarov, P., Andonov, B., & Pancheva, D. (2013). Global empirical model of TEC response to geomagnetic activity. *Journal of Geophysical Research Space Physics*, *118*, 1–20.
- Ouzounov, D., Liu, D., Chunli, K., Cervone, G., Kafatos, M., & Taylor, P. (2007). Outgoing long wave radiation variability from IR satellite data prior to major earthquakes. *Tectonophysics*, *431*(1–4), 211–220.
- Pedatella, N. M., Lei, J., Larson, K. M., & Forbes, J. M. (2009). Observations of the ionospheric response to the 15 December 2006 geomagnetic storm: long-duration positive storm effect. *Journal of Geophysical Research Space Physics*. doi:10.1029/2009JA014568.
- Piroddi, L., & Ranieri, G. (2012). Night thermal gradient: a new potential tool for earthquake precursors studies. An application to the seismic area of L'Aquila (Central Italy). *Selected Topics in Applied Earth Observations and Remote Sensing*, *5*(1), 307–312.
- Přša, D., Parrot, M., & Santolík, O. (2011). Ionospheric density variations recorded before the 2010 Mw 8.8 earthquake in Chile. *Journal of Geophysical Research*. doi:10.1029/2011JA016611.
- Pulinets, S. A., & Boyarchuk, K. (2004). *Ionospheric precursors of earthquakes* (p. 316). Berlin: Springer.
- Pulinets, S. A., & Davidenko, K. (2014). Ionospheric precursors of earthquakes and global electric circuit. *Advances in Space Research*, *53*(5), 70–723.
- Pulinets, S. A., & Ouzounov, D. (2011). Lithosphere-atmosphere-ionosphere coupling (LAIC) model—an unified concept for earthquake precursors validation. *Journal of Asian Earth Sciences*, *41*(4–5), 371–382.
- Pulinets, S. A., Ouzounov, D., Karelin, A., & Davidenko, D. (2014). Physical bases of the generation of short-term earthquake precursors: a complex model of ionization-induced geophysical processes in the lithosphere–atmosphere–ionosphere–magnetosphere system. *Geomagnetism and Aeronomy*, *55*(4), 522–539.
- Pulinets, S. A., Romanov, A. A., Urlichich, Y. M., Romanov, A., Doda, L. N., & Ouzounov, D. (2009). The first results of the pilot project on complex diagnosing earthquake precursors on Sakhalin. *Geomagnetism and Aeronomy*, *49*(1), 115–123.
- Qin, K., Wu, L., Liu, S., De Santis, A., & Cianchini, G. (2012). Mechanisms and relationship to soil moisture of surface latent heat flux anomaly before Inland earthquakes. In *Proceeding of geoscience and remote sensing symposium (IGARSS)*, IEEE.
- Rozhnoi, A., Solovieva, M., Molchanov, O. A., Biagi, P. F., & Hayakawa, M. (2007). Observation evidences of atmospheric Gravity Waves induced by seismic activity from analysis of subionospheric LF signal spectra. *Natural Hazards and Earth System Science*, *7*, 625–628.
- Rycroft, M. J., & Harrison, R. G. (2012). Electromagnetic atmosphere-plasma coupling: the global electric circuit. *Space Science Reviews*, *168*(1–4), 363–384.
- Rycroft, M. J., Harrison, R. G., Nicoll, K. A., & Mareev, E. A. (2008). An overview of Earth's global electric circuit and atmospheric conductivity. *Space Science Reviews*, *137*(1–4), 83–105.
- Sapkota, B. K., & Varshneya, N. C. (1990). On the global atmospheric electrical circuit. *Journal of Atmospheric and Solar Terrestrial Physics*, *52*(1), 1–20.
- Schaer, S., Gurtner, W., & Feltens, J. (1998). IONEX: the IONosphere map exchange format version 1. In *Proceedings of the 1998 IGS analysis centers workshop*, ESOC, Darmstadt, Germany.
- Scoville, J., Sornette, J., & Freund, F. T. (2015). Paradox of peroxy defects and positive holes in rocks Part II: outflow of electric currents from stressed rocks. *Journal of Asian Earth Sciences*, *114*(2), 338–351.
- Silva, H. G., Bezzeghoud, M., Reis, A. H., Rosa, R. N., Tlemçani, M., Araújo, A. A., et al. (2011). Atmospheric electrical field

- decrease during the $M = 4.1$ Sousel earthquake (Portugal). *Natural Hazards and Earth System Sciences*, 11, 987–991.
- Singh, A. K., Siingh, D., Singh, R. P., & Mishra, S. (2011). Electrodynamical coupling of earth's atmosphere and ionosphere: an overview. *International Journal of Geophysics*, 971302, 971313.
- Sykes, L. R., Shaw, B. E., & Scholz, C. H. (1999). Rethinking earthquake prediction. *Pure and Applied Geophysics*, 155, 207–232.
- Takagi, M., & Kanada, M. (1972). Global variation in the atmospheric electric field. *Pure and Applied Geophysics*, 100(1), 44–53.
- Thomas, J. N., Holzworth, R. H., & McCarthy, M. P. (2009). In situ measurements of contributions to the global electrical circuit by a thunderstorm in southeastern Brazil. *Atmospheric Research*, 91, 153–160.
- Tyrtshinikov, A. V. (1996). The variations of ozone content in the atmosphere above strong earthquake epicenters. *Physics of the Solid Earth*, 31(9), 789–794.
- United States Geological Survey (2015). Technical report of M8.3–48 km W of Illapel, Chile 2015-09-16 22:54:32 UTC. United States Geological Survey.
- Walia, V., Virk, H. S., & Bajwa, B. S. (2006). Radon precursory signals for some earthquakes of magnitude >5 occurred in N–W Himalaya: an overview. *Pure and Applied Geophysics*, 163(4), 711–721.
- Yada, N., & Saito, Y. (2012). Precursor observed by movements of aero-ionization measurement prior to the pacific coast of Tohoku earthquake in 2011. In EMSEV 2012, edited, p 5, Gotemba, Japan
- Yagi, Y., Okuwaki, R., Enescu, B., Hirano, S., Yamagami, Y., Endo, S., et al. (2014). Rupture process of the 2014 Iquique Chile Earthquake in relation with the foreshock activit. *Geophysical Research Letters*, 41(2), 4201–4206.
- Zhang, X., Zeren, Z., Parrot, M., Battiston, R., Qian, J., & Shen, X. (2011). ULF/ELF ionospheric electric field and plasma perturbations related to Chile earthquakes. *Advances in Space Research*, 47(6), 991–1000.
- Zlotnicki, J., Li, F., & Parrot, M. (2012). Ionospheric disturbances recorded by DEMETER satellite over active volcanoes: from August 2004 to December 2010. *International Journal of Geophysics*, 2013, 1–17. (ID 530865, 530817).

(Received May 2, 2016, revised July 25, 2016, accepted July 26, 2016, Published online August 18, 2016)